Analysis Note

Centrality dependence of directed flow v_1 of protons in the Xe+Cs(I) collisions at 3.8 AGeV (BM@N run8)

Valery Troshin[1], Alexander Demanov [2], Petr Parfenov, Oleg Golosov, Mikhail Mamaev, Fedor Karpushkin, Irina Zhavoronkova, Sergey Sedykh, Mikhail Rumyantsev, Arkadiy Taranenko[3]

National Research Nuclear University MEPhI, Moscow, Russia
Joint Institute for Nuclear Research, Dubna, Russia

In this note, we present the new results of the measurements of directed flow (v_1) of protons from Xe+Cs(I) collisions at 3.8 AGeV (BM@N run8). We show the datasets, event and track selection cuts, centrality definition, event plane reconstruction and resolution. The analysis procedure for anisotropic flows is completely identical to that in the previous work [1]. The v_1 results are presented as function of centrality for selected bins in transverse momentum (p_T) and rapidity (y_{cm}). The systematic uncertainty study will also be presented and discussed.

The work has been supported by the Ministry of Science and Higher Education of the Russian Federation, Project "Fundamental and applied research at the NICA(JINR) megascience experimental complex" № FSWU-2025-0014.

---

[1]E-mail: valerytrosh@gmail.com
[2]E-mail: demanov1997@gmail.com
[3]E-mail: ataranenko.ru

Contents

1 Introduction **3**

2 Analysis details **8**

2.1 The layout of the BM@N experiment 8

2.2 Quality Assurance (QA) study 10

2.3 Data, Event and Track Selection 12

2.4 Identification of protons 13

3 Centrality determination **17**

3.1 Event and Track Selection Criteria 17

3.2 Centrality Estimation via the Glauber Monte Carlo Method 17

3.3 Centrality estimation via direct reconstruction method 19

3.4 Run-by-Run Multiplicity Correction 23

3.5 Efficiency Evaluation 28

3.6 Estimation of the Off-Target Collision Fraction 33

4 Methods for analyzing anisotropic flow in BM@N **40**

4.1 General framework for the flow measurements 40

4.2 The analysis of v_1 of protons from BM@N run8 data 46

4.3 Systematic uncertainties of v_1 measurements 49

5 Results of the directed flow measurements **50**

1 Introduction

Relativistic heavy-ion collisions can directly generate the high density and/or temperature strong interacting matter, and thus provide the opportunity to explore the strong interaction properties at extreme conditions. One of the interests is the exploration of nuclear Equation of State (EoS) as well as the symmetry energy for asymmetric nuclear matter at high densities [2]. The anisotropic collective flow of final state particles is a direct reflection of the pressure and its gradients created in relativistic heavy-ion collisions and thus is closely related to the EoS of dense matter. The anisotropic flow can be quantified by Fourier coefficients v_n [3–6] in the expansion of the particle azimuthal distribution relative to the reaction plane given by the angle Ψ_R:

$$dN/d\phi \propto 1 + \sum_{n=1} 2v_n \cos(n(\varphi - \Psi_R)), \tag{1}$$

where n is the order of the harmonic and φ is the azimuthal angle of a particle of the given type. The flow coefficients v_n can be calculated as $v_n = \langle \cos[n(\varphi - \Psi_R)] \rangle$, where the brackets denote the average over the particles and events. The directed (v_1) and elliptic (v_2) flows are dominant and most studied signals in the energy range of $2 < \sqrt{s_{\rm NN}} < 5$ GeV [7–13]. The comparison of existing measurements of v_1 and v_2 of protons and light fragments in Au+Au collisions at $\sqrt{s_{\rm NN}}$ = 2.07-4.72 GeV (corresponding to beam energies E_{beam}=0.4-10 AGeV) with results from hadronic transport simulations provides the most stringent currently available constraints on the high-density EOS of symmetric nuclear matter [2; 14; 15], see the right panel of Figure 1. At densities between 1 and 2 times saturation density ρ_0, the v_2 data for protons, deuterons and tritons in Au+Au collisions measured at E_{beam} = 0.4–1.49 AGeV ($\sqrt{s_{\rm NN}}$ = 2.07-2.51 GeV) by the FOPI experiment at GSI [10] have been used together with IQMD model transport calculations to constrain the nuclear incompressibility K_{nm} [16]. The model that takes into account momentum-dependent interactions, can explain the data with a fairly soft EOS (K_{nm}=190 $\pm$ 30 MeV) [15], see the solid yellow region in the right panel of Figure 1.

At densities ~2-5 ρ/ρ_0, the comparison of the existing v_1 and v_2 measurements

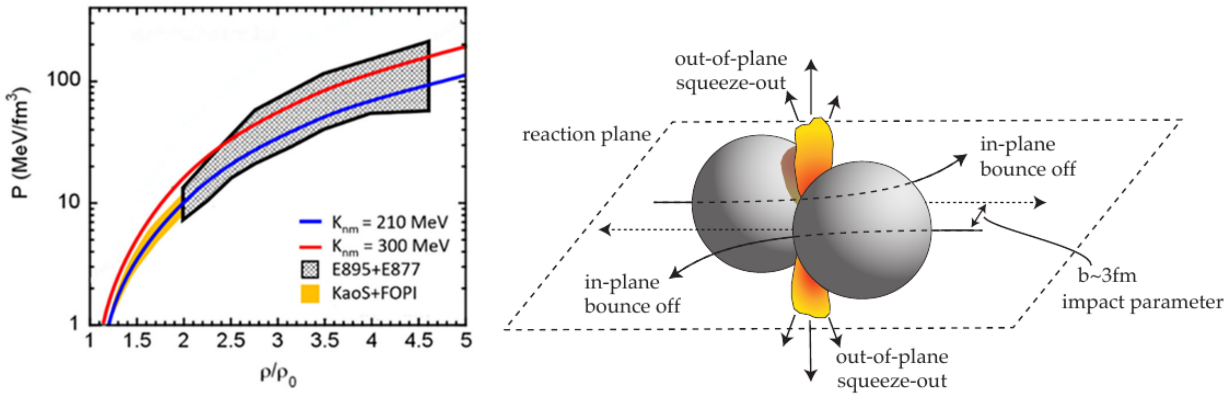

Figure 1: Left panel: Pressure as function of baryon density for symmetric nuclear matter. Selected constraints on the symmetric EOS obtained from comparisons of experimental flow data to hadronic transport simulations, see text for the details. The figure is taken from [15]. Right panel: Illustration of a semi-central collision of two nuclei with an impact in the $\sqrt{s_{\rm NN}}$ = 2.0-3.5 GeV energy regime, with the direction of the flow phenomena indicated with arrows into ($v_1 > 0$ or "bounce-off" of spectators) or perpendicular ($v_2 < 0$ or "squeeze-out") to the reaction plane.

of protons in Au+Au at E_{beam} = 2–8 AGeV ($2.5 < \sqrt{s_{\rm NN}} < 4.5$ GeV) by the E895 experiment at AGS [7–9] with results of microscopic transport models leads to the values of nuclear incompressibility K_{nm} = 200-380 MeV [14], depicted by the grey hatched region in Figure 1. The description of v_1 results from E895 experiment requires a soft EOS with the incompressibility K_{nm} = 200 MeV, while reproducing the v_2 data required larger values of K_{nm} = 380 MeV (and therefore a harder EOS). A Bayesian analysis study [17] suggests a difference between the E895 [7–9] and recently obtained STAR [12; 13] data from RHIC Beam Energy Scan program. Using only the STAR measurements, the study [17] further found that the slope of the directed flow and the elliptic flow of protons can be described by thy transport model with the same EOS. The E895 flow measurements [7–9] have been performed 15-20 years ago by the standart event plane method, which do not take into account the influence of non-flow effects on v_n measurements [18]. Therefore, high-precision measurements of anisotropic flow at $2 < \sqrt{s_{\rm NN}} < 5$ GeV with a modern methods of analysis are required, in order to further constrain the EOS of symmetric matter from model comparisons [15; 18].

The important characteristic of this energy range is that the compressed overlap

zone expands at the time t_{exp} comparable to the passage time t_{pass}, at which the accelerated nuclei interpenetrate each other. The expansion time $t_{exp} \sim R/c_s$ is governed by a fundamental property, the speed of sound c_s which connects to the EOS [9; 14]. The passage time t_{pass} can be estimated as $t_{pass} = 2R/sinh(y_{beam})$, where R is the radius of the nucleus and y_{beam} is the beam rapidity [8; 9; 14]. For Au+Au collisions at $2.4 < \sqrt{s_{\rm NN}} < 5$ GeV, the t_{pass} decreases from 18 fm/c to 6 fm/c. If the passage time is long compared to the expansion time, spectator nucleons serve to block the path of produced hadrons emitted towards the reaction plane. Such rather complex collision geometries result in strong change in the resulting flow patterns. For example, for Au+Au collisions at $\sqrt{s_{\rm NN}} < 3.3$-3.5 GeV, the nuclear matter is "squeezed-out" perpendicular to the reaction plane giving rise to negative elliptic flow ($v_2 < 0$) and squeeze-out contribution should then reflect the ratio $c_s/sinh(y_{beam})$ [9; 14], see the right panel of Figure 1. The t_{pass} depends on the size of colliding system and beam energy. Therefore, the study of the system size dependence of anisotropic flow may help to estimate the participant-spectator contribution and improve our knowledge of EOS of symmetric nuclear matter.

The Baryonic Matter at the Nuclotron (BM@N)[19] is a fixed target experiment at JINR (Dubna), In February 2023, the first physics run of the BMN experiment was completed with recorded Xe + Cs(I) collision events at 3.8 AGeV ($\sqrt{s_{\rm NN}} = 3.26$ GeV). In 2024–2025, the first results of measuring the directed flow v_1 of protons and deuterons in mid-central (10–30%) Xe + Cs(I) collisions were obtained. As an example the left panel of Fig. 2 shows the preliminary results of directed flow v_1 of protons in 10-30% central Xe+Cs(I) collisions at 3.8 A GeV as a function of rapidity y_{cm}. The resulting values of the slope of v_1 of protons and deuterons at midrapidity $dv_1/dy_{cm}|_{y_{cm}=0}$ as a function of collision energy is presented in the right panel of Fig. 2. The results for the BM@N experiment are compared with existing data from other experiments [10; 13; 20]. Directed flow slope at midrapidity $dv_1/dy_{cm}|_{y_{cm}=0}$ are found to be in a reasonable agreement with the existing measurements. The details of the analysis of v_1 of protons can be found the following analysis note [1]:
https://indico.jinr.ru/event/4750/attachments/19780/34163/ANoteFlowRun8.pdf
The slope of v_1 of protons at mid-rapidity $dv_1/dy|_{y=0}$ exhibits no significant centrality dependence for all p_T intervals, except for the very central class where $dv_1/dy|_{y=0}$ is

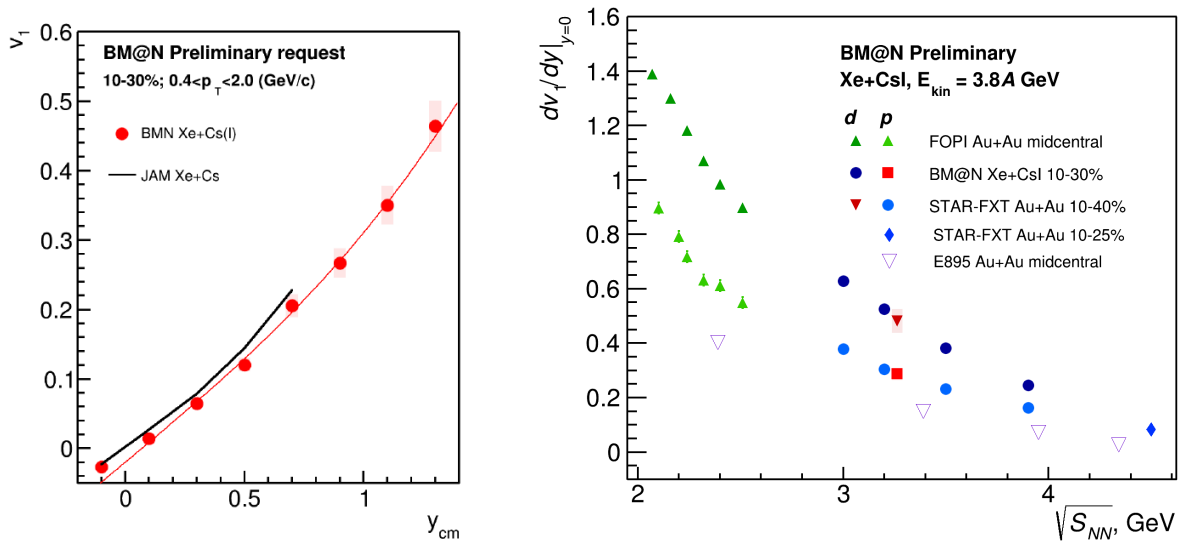

Figure 2: Left panel: directed flow v_1 of protons in 10-30% central Xe+Cs(I) collisions at 3.8 A GeV as a function of rapidity y_{cm}. Right panel: the slope of v_1 of protons and deuterons at midrapidity $dv_1/dy_{cm}|_{y_{cm}=0}$ as a function of collision energy. The obtained BM@N results were compared with existing data from other experiments.

smaller than for the other centralities, see left panel of Figures 3 and upper panel of Figure 4. In contrast, the v_2 signal of protons has a strong (almost linear) dependence on centrality, see right panel of Figure 3 and lower panel of Figure 4. The fluctuations of v_1 and v_2 may lead to non-zero values in the most central collisions. The published results for centrality dependence of v_1 of protons are available only for Au+Au collisions at $\sqrt{s_{NN}}$= 2.4 GeV (HADES), the STAR results for Au+Au collisions at $\sqrt{s_{NN}}$ = 3 GeV are still preliminary. There are no published measurements in the 2.5–3.5 GeV energy range.

In this analysis note, we present first results for centrality dependence of directed flow (v_1) of protons in Xe + Cs(I) collisions at E_{beam} = 3.8 AGeV. The analysis procedure for anisotropic flows is completely identical to that in the previous work [1]. The v_1 results are presented as function of centrality for selected bins in transverse momentum (p_T) and rapidity (y_{cm}). The note is organized as follows. Section 2 introduces the BM@N experimental set-up, QA study, the centrality and the particle identification methods, while section 3 discusses the procedures used to determine the v_1 of protons and systematic uncertainty study. Section 4 presents the main results on directed flow v_1 of protons.

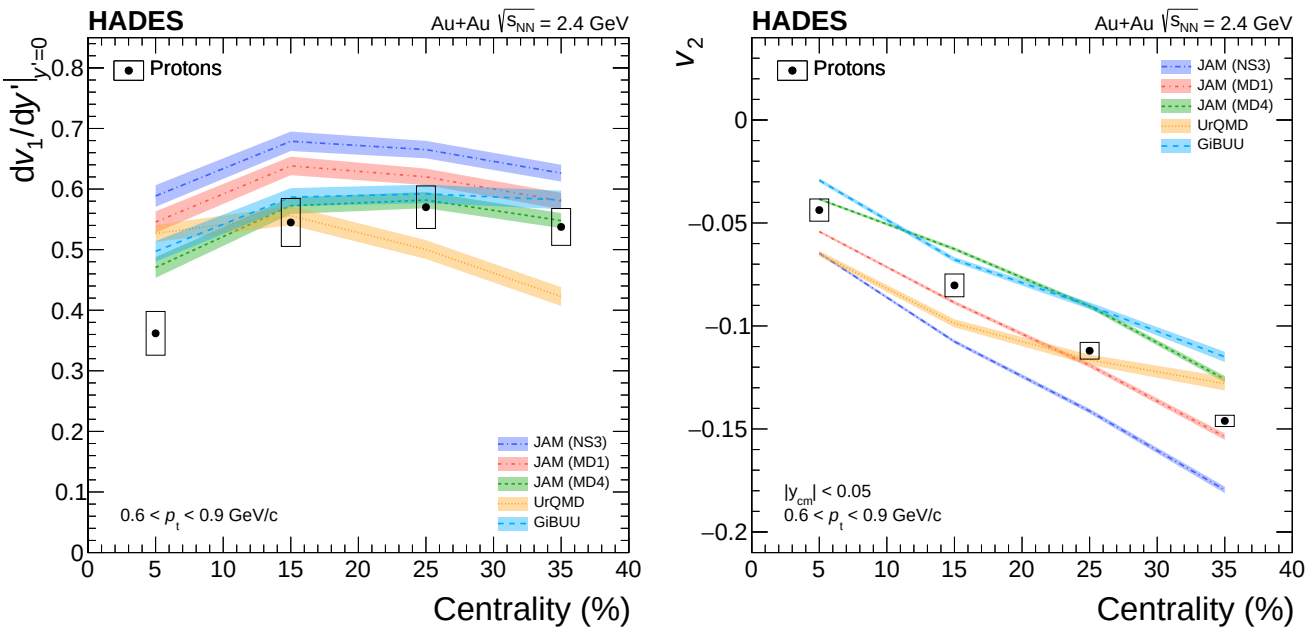

Figure 3: The slope $dv_1/dy'|_{y'=0}$ (left panel) and elliptic v_2 (right panel) flow of protons in the interval $0.6 < p_T < 0.9$ GeV/c at mid-rapidity in Au+Au collisions at $\sqrt{s_{NN}}$= 2.4 GeV for four centrality classes. The HADES data are compared to several model predictions. The figure is taken from [11]

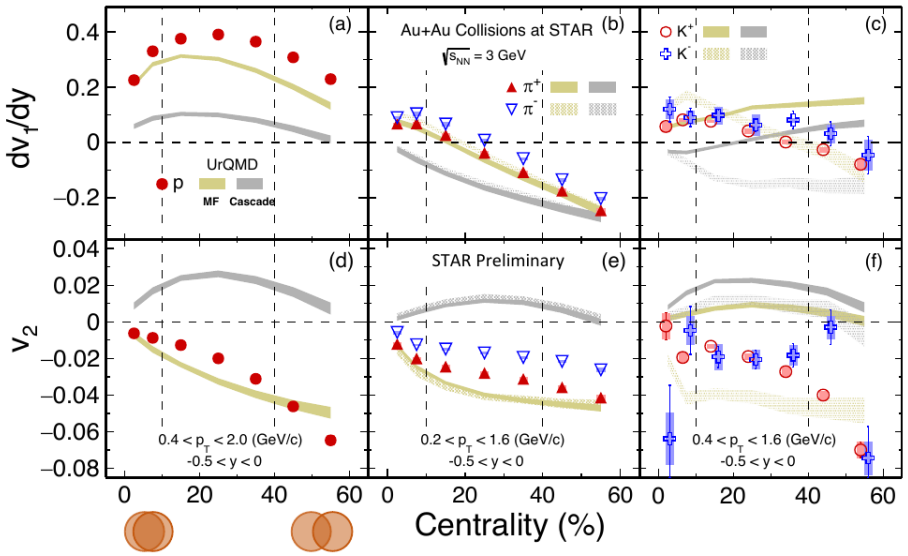

Figure 4: The centrality dependence of the slope $dv_1/|_{y=0}$ (upper panel) and elliptic v_2 (lower panel) flow of protons, pions and kaons at mid-rapidity in Au+Au collisions at $\sqrt{s_{NN}}$= 3.0 GeV. The STAR data are compared to UrQMD model prediction. The figure is taken from [13; 20]

2 Analysis details

This section briefs about the related details for analysis of the experimental data for Xe+Cs(I) collisions at 3.8 AGeV (BM@N run8), such as the selection of good events and tracks for analysis, particle identification used for selecting protons, and the definition of collision centrality for geometry of collisions. Prior to conducting physical analysis, the data underwent a thorough evaluation to ensure that only good runs were included, called run-by-run Quality Assurance (QA).

2.1 The layout of the BM@N experiment

The BM@N detector is a forward spectrometer that covers the pseudorapidity range $1.6 \leq \eta \leq 4.4$ [19]. The layout of the BM@N experiment for the Xe+Cs(I) run8 is shown in the Figure 5. The main subsystems of the BM@N [19] are the tracking system for charged hadron tracking, the Time Of Flight (TOF) system for charged particle identification and the set of forward detectors for centrality and reaction plane estimations. The tracking system is comprised of 4 stations of the Forward Silicon Detector (FSD) and 7 stations of Gaseous Electron Multipliers (GEM) chambers mounted downstream of the silicon sensors, see left part of Figure 5. Both the silicon tracking system (FSD) and the GEM stations will be operated in the magnetic field (at maximum value of 1.2 T) of a large aperture dipole magnet and allow the reconstruction of the momentum p of charged particles. The z axis of the BM@N coordinate system is directed along the beam line, while the magnetic field is directed along the y axis. The FSD+GEM system provides also the measurements of the multiplicity of the produced charged particles N_{ch}, which can be used as an estimator of the collision centrality.

The TOF-system consists of 3 planes of multi-gap Resistive Plate Chambers (mRPC) placed at $z = 400$ and $z = 700$ cm (TOF-400 and TOF-700, respectively) from the target, see the central part of Figure 5. The detectors BC1 and BC2 define the start time for the time-of-flight system. Three forward detectors: Forward Hadronic Calorimeter (FHCal), quartz hodoscope (Hodo) and Scintillator Wall (ScWall) provide the information about the spectator fragments, see the right part of the Figure 5. FHCal provides the information about the energy of spectators

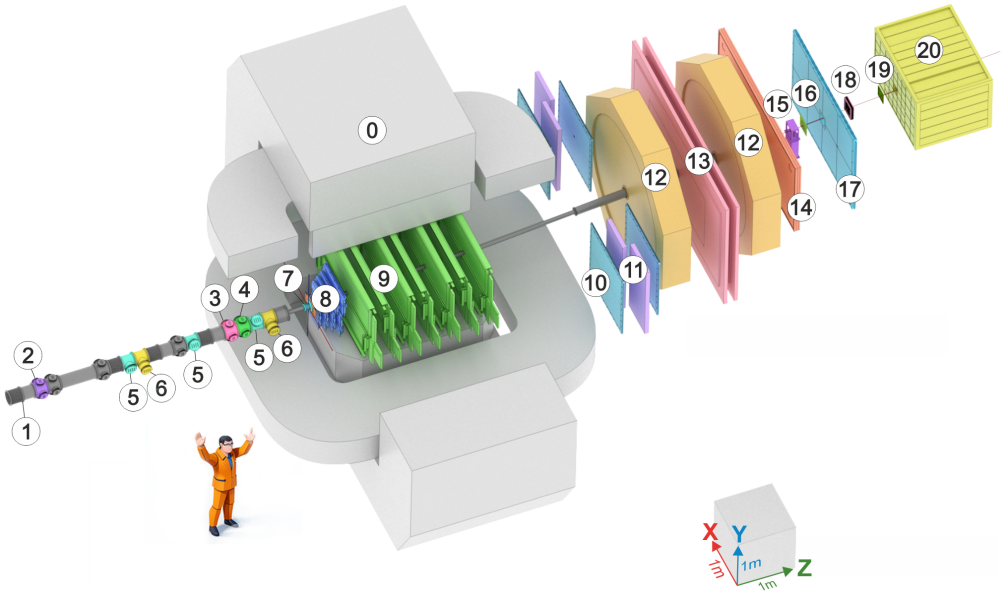

Figure 5: The layout of the BM@N experiment for the Xe+Cs(I) run8 2022-2023. Main components: (0) SP-41 analyzing magnet, (1) vacuum beam pipe, (2) BC1 beam counter, (3) Veto counter (VC), (4) BC2 beam counter, (5) Silicon Beam Tracker (SiBT), (6) Silicon beam profilometers, (7) Barrel Detector (BD) and Target station, (8) Forward Silicon Detector (FSD), (9) Gaseous Electron Multiplier (GEM) detectors, (10) Small cathode strip chambers (Small CSC), (11) TOF400 system, (12) drift chambers (DCH), (13) TOF700 system, (14) Scintillation Wall (ScWall), (15) Fragment Detector (FD), (16) Small GEM detector, (17) Large cathode strip chamber (Large CSC), (18) gas ionization chamber as beam profilometer, (19) Forward Quartz Hodoscope (FQH), (20) Forward Hadron Calorimeter (FHCal). The figure is taken from [19]

fragments and consists of 54 modules. The modules have sampling structure and consist of a set of lead and scintillator plates compressed together by a steel band. FHCal has a 15 x 15 cm^2 square beam hole in the center. The beam hole leads to the leakage of the fragments with small transverse momenta. As a result, the deposited energy in the FHCal is comparable for the central and peripheral events. This creats an ambiguity in the dependence of energy deposition on the collision centrality. New forward quartz hodoscope (Hodo) has been developed to be placed in the beam hole to measure the energy of spectator fragments. It helps to compensate the effect due to the leakage of the heavy fragments mostly in the peripheral collisions. ScWall has a wider acceptance than FHCal and provides information about the charge of spectator fragments.

2.2 Quality Assurance (QA) study

The collection of events for a collision energy is done over several discrete time spans. Each of these time spans where the detector was continuously recording events is called a "run" and it can be selected by RunId. Each run consists of event and track information of the heavy-ion collisions recorded by the BM@N detector. We perform quality assurance (QA) checks for the selection of good runs. Averaged QA observables like: N_{ch} (charged particle multiplicity in FSD+GEM system), E_{tot} (total energy of spectator fragments in the FHCal), N_{vtx} (number of tracks in the vertex reconstruction), etc., are calculated for each run. Then, the mean (μ) and standard deviation (σ) are calculated for the distribution of selected observables Y as a function of RunId:

$$\mu = \frac{1}{N}\sum_{i=1}^{N} Y_i \tag{2}$$

$$\sigma = \sqrt{\frac{1}{N}\sum_{i=1}^{N}(Y_i - \mu)^2}, \tag{3}$$

where i - RunId number and N - total numbers of runs. The runs for which the averaged QA observables lie beyond $\pm 3\sigma$ away from their global means are identified as bad runs, and all the events from that run are removed from the analysis. As an example Figure 6 shows the RunId dependence of the mean number of FSD and GEM digits. Black dotted horizontal line and red horizontal lines represent μ and $\pm 3\sigma$, respectively.

The detailed analysis note with all results of QA study can be found at:

http://indico.oris.mephi.ru/event/315/contribution/1/material/slides/0.pdf

The list of bad runs based on QA study [18M events] RunId:

6968, 6970, 6972, 6973, 6975, 6976, 6977, 6978, 6979, 6980, 6981, 6982, 6983, 6984,7075, 7076, 7077, 7078, 7081, 7083, 7084, 7086, 7087, 7091, 7092, 7093, 7096, 7097, 7098, 7100, 7101, 7102, 7103, 7104, 7313, 7326, 7415, 7417, 7435,7469, 7471, 7517, 7519, 7520, 7537, 7538, 7542, 7543, 7545, 7546, 7547, 7573, 7575, 7657, 7659, 7679, 7681, 7843, 7847, 7848, 7850, 7851, 7852, 7853, 7855, 7856, 7857, 7858,

7859, 7865, 7868, 7869, 7907, 7910, 7932, 7933, 7935, 7937, 7954, 7955, 8018, 8028, 8029,8030, 8031, 8032, 8033, 8115, 8121, 8167, 8201, 8202, 8203, 8204, 8205, 8206, 8207, 8208, 8209, 8210, 8211, 8212, 8213, 8215, 8284, 8281, 8289.

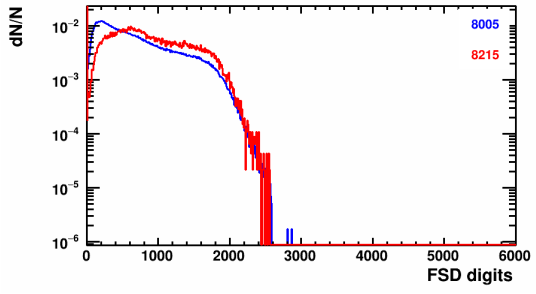

(a)

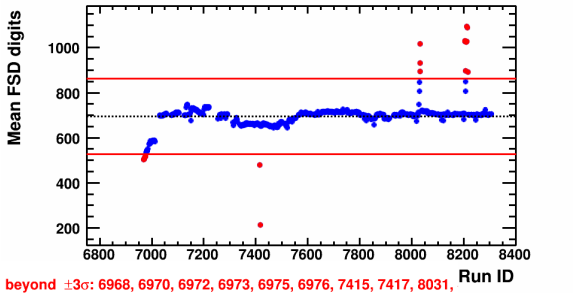

(b)

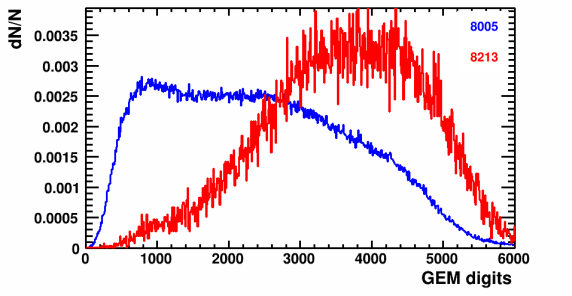

(c)

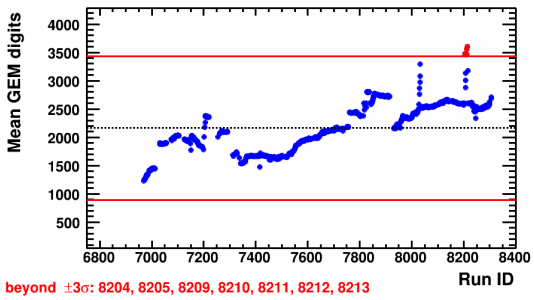

(d)

Figure 6: Distribution of the number of digits in the FSD (a) and GEM (c) detectors. The red marker corresponds to the distribution from the "outlier" RunId. Mean number of FSD digits (b) and GEM digits (d) as a function of RunID (right panel). Black dotted horizontal line and red horizontal lines represent μ and $\pm 3\sigma$, respectively.

2.3 Data, Event and Track Selection

In total approximately 500 million events of Xe+Cs(I) collisions at the beam energy of 3.8A GeV were collected by the BM@N experiment in the January of 2023. The official production build from Sep 25 (the latest one to date) was used.
1) We don't consider runs below RunId=7050 due to unstable operation of the GEM and FSD detectors (BM@N Electronic Logbook) and QA study.
2) We removed 74 runs [18M events] based on QA study, see section 3.2
3) We used events from Physical runs and CCT2 trigger [19].
4) at least 2 tracks in vertex reconstruction
5) The pileup events were rejected based on the procedure explained in details in the Oleg Golosov analysis note:
http://indico.oris.mephi.ru/event/314/contribution/0/material/0/0.pdf
6) The event vertex is defined by MpdVertex, calibrated to be centered at zero for each run, and is subject to the following constraints: $|VtxZ| < 1$ cm, VtxR< 1 cm (in the XY plane).
7) The total number of events after all selections is 171 million.

Selection criteria are also imposed on tracks to ensure good tracks for analysis. The selection cuts applied are as follows:
1) Tracks of charged particles were selected based on the number of stations N_{hits} in the BM@N inner tracking system used for track reconstruction. At least 6 were required to satisfy the criteria of a good track: $N_{hits} \geq 6$.
2) Only tracks with fit quality $\chi^2/NDF < 5$ were analyzed.
3) Distance of the closest approach (DCA) of tracks from the primary vertex in the direction perpendicular to the beam: DCA < 5 cm

2.4 Identification of protons

Protons are identified using the time of flight Δt measured between T0 and the ToF detectors, the length of the trajectory ΔL and the momentum p reconstructed in the BM@N central tracker. Then the squared mass m^2 of a particle is calculated. The original calibration of T0 offsets for TOF-400 and TOF-700 detactors was done using one group of runs. As a result, a rather large spread in the mean values of the T0 distribution (time minus the expected proton time-of-flight) vs. RunID can be observed, see Figure 7 (closed circles).

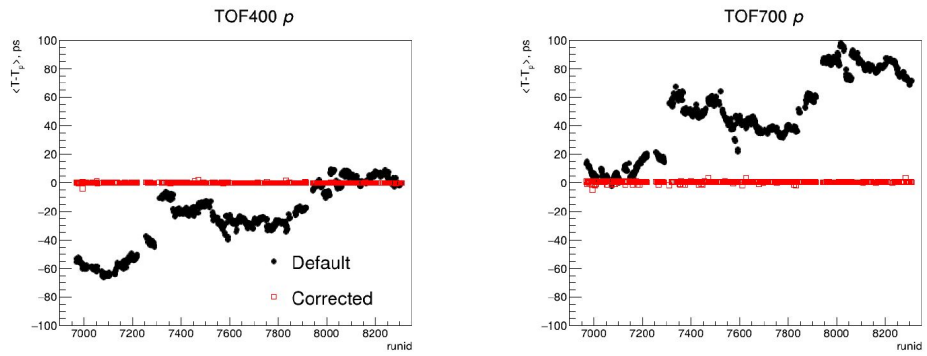

Figure 7: Mean values of the T0 distribution (time minus the expected proton time-of-flight) vs RunID for TOF-400 and TOF-700 before (closed circles) and after calibration (open boxes).

An additional calibration of the TOF detectors was performed; details can be found in the following note: https://indico.jinr.ru/category/913/attachments/26261/47301/AnalysisNote_PDF_Version.pdf The open boxes in Figure 7 show the RunID dependence of mean values of the T0 distribution after calibration.

For each bin in momentum the position $\langle m_p^2 \rangle$ and the width $\sigma_{m_p^2}$ of the proton m^2 peak was extracted from the Gaussian fit. The procedure was done separately for TOF-400 and TOF-700 as they have different timing resolution. The proton samples selected by the requirements of $(m^2\text{-}\langle m_p^2 \rangle) < 3\sigma_{m_p^2}$, see Figures 8–9.

Figure 10 shows the phase space coverage of identified protons as a function of rapidity y_{cm} and transverse momentum p_T for combined system TOF-400 and TOF-700. Optimized cut on extrapolation coordinates to FHCal plane have a significant effect on size of the statistics and acceptance form, see right panel of Figure 10. Efficiency of the proton reconstruction was calculated using the realistic Monte-

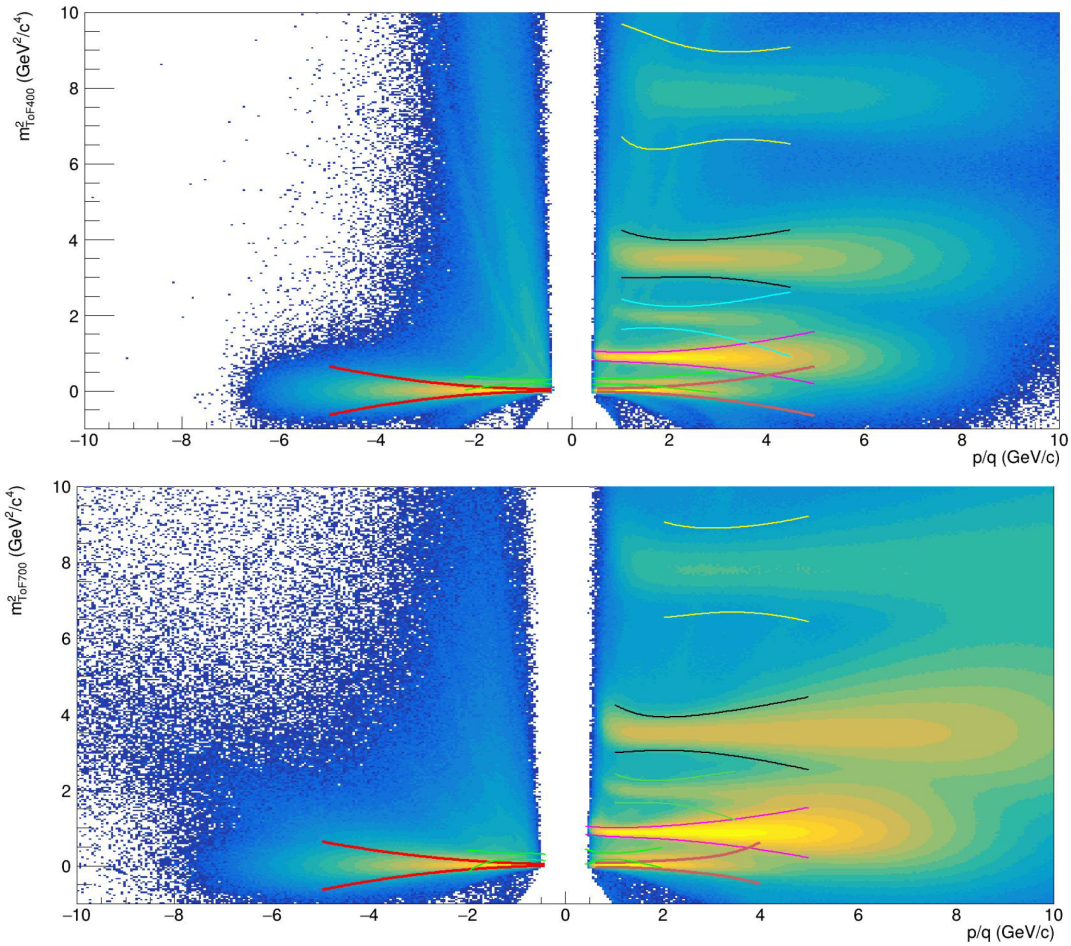

Figure 8: Population of selected protons in the m^2 vs. rigidity (p/q) plane for TOF400 (upper panel) и TOF700 (lower panel). The upper and lower boundaries of the identification areas for different particle species are shown by colored lines and defined as m^2-$\langle m_p^2 \rangle) < 3\sigma_{m_p^2}$

Carlo modelling of the BM@N experiment using GEANT4 transport code and JAM in the mean field mode events as an input. Efficiency of the proton reconstruction with the TOF-detectors acceptance applied.

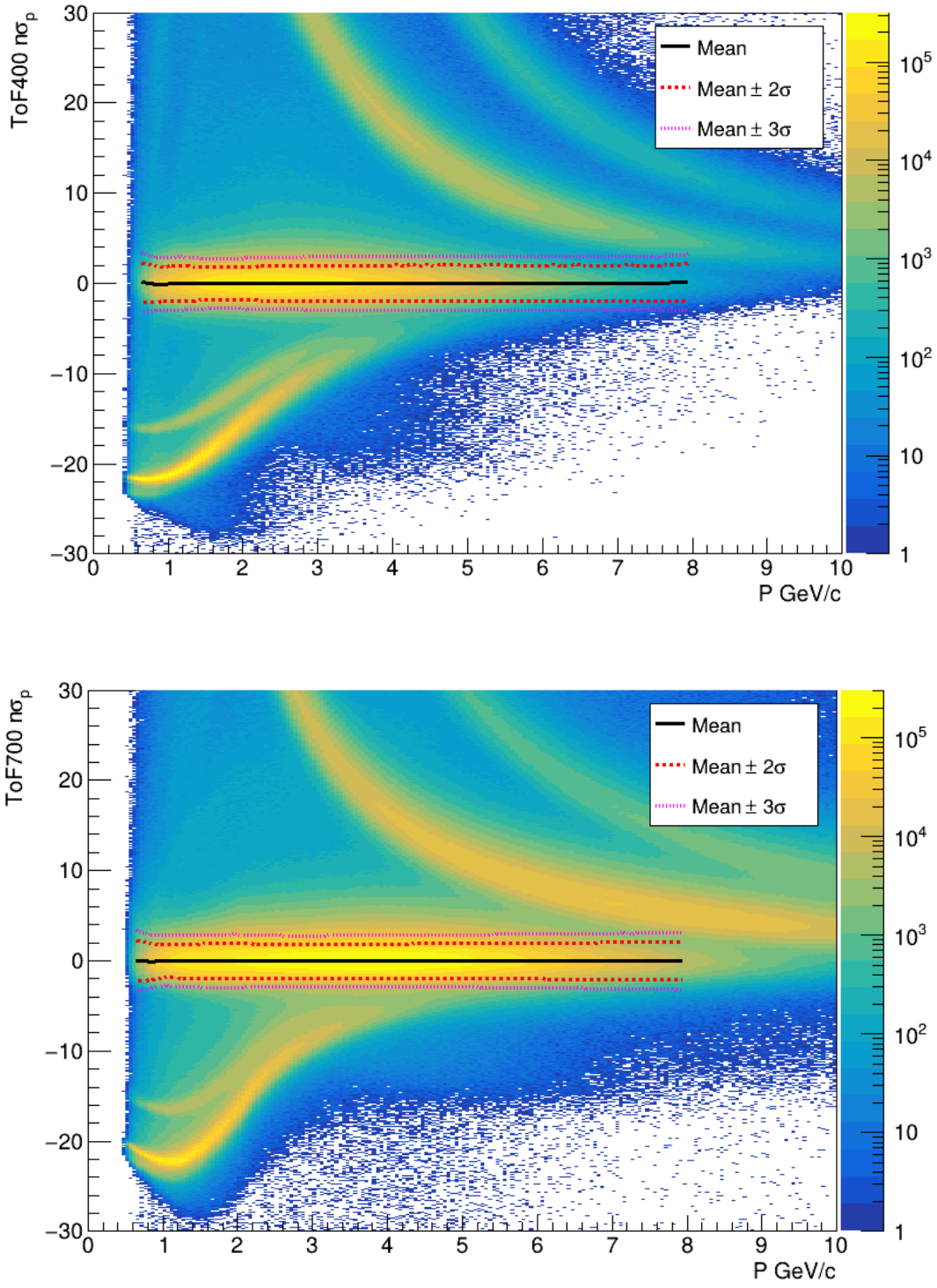

Figure 9: $n\sigma$ distributions for protons as a function of p/q for TOF400 (upper panel) и TOF700 (lower panel). Different lines shows the selection cuts : $n\sigma = \pm 2$ and $n\sigma = \pm 3$.

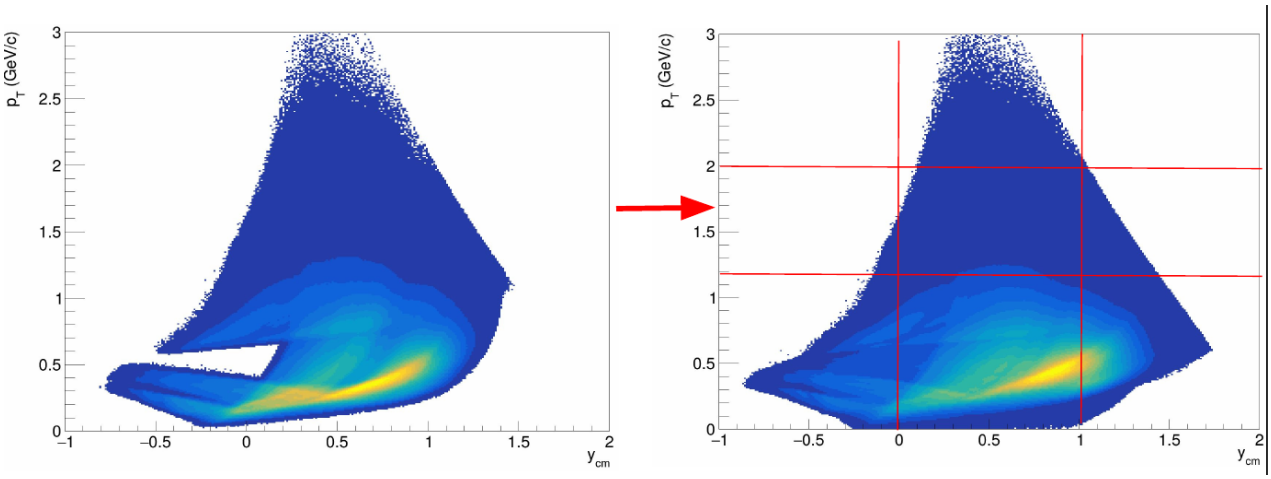

Figure 10: The phase space coverage of identified protons as a function of the centre-of-mass rapidity y_{cm} and transverse momentum p_T with original cuts (left panel) and after improved selection cuts (right panel).

3 Centrality determination

3.1 Event and Track Selection Criteria

The analysis utilized data from the first BM@N physics run with the full configuration of detector systems (Run 8), obtained in collisions of xenon ions (Xe) with a Cs(I) target at a beam kinetic energy of $3.8A$ GeV, which corresponds to $\sqrt{s_{NN}} \simeq 3.26$ GeV. Events were considered if the primary vertex position was reconstructed using more than 1 track within 1 cm along the z-axis and within $\mu_{x,y} \pm 1.5$ cm along the xy-axes for each event sample. When constructing the multiplicity distribution (RefMult), only tracks associated with the primary vertex were used. The following kinematic and geometric selection criteria were applied to them: distance of closest approach (DCA) of the track to the primary vertex $|\mathrm{DCA}| < 1$ cm, transverse momentum $0.05 < p_T < 2$ GeV/c, and pseudorapidity $0.7 < \eta < 2.5$.

3.2 Centrality Estimation via the Glauber Monte Carlo Method

An improved version of the PHOBOS Glauber Monte Carlo software implementation [21] was utilized to determine centrality based on charged particle multiplicity. The model simulates the geometry of each nucleus-nucleus collision and, for a given impact parameter b, computes the number of participating nucleons N_{part} and binary nucleon-nucleon collisions N_{coll}.

The spatial distribution of nucleons was specified by a two-parameter Fermi distribution:

$$\rho(r) = \frac{\rho_0}{1 + \exp[(r - R)/a]}, \tag{4}$$

where R is the effective nuclear radius, a is the surface skin depth (diffuseness), and ρ_0 is determined by the normalization condition to the total number of nucleons.

The calculations incorporated the experimental system $\mathrm{Xe}^{124} + \mathrm{CsI}$. The parameters of the colliding nuclei were specified directly within the MC-Glauber code: for ^{124}Xe — $N = 124$, $Z = 54$, $R = 5.431$ fm, $a = 0.5978$ fm, $\beta_2 = 0.212$, $\beta_4 = -0.018$ (ALICE parameters [22]); for CsI — $N = 130$, $Z = 54$, $R = 6.07$ fm,

$a = 0.5$ fm, $\beta_2 = \beta_4 = 0$. Thus, R, a, and the deformations were predefined prior to the fitting process and governed the geometric component of the calculation.

Nucleons travel along straight-line trajectories, and the nucleus-nucleus interaction is represented as a sequence of independent binary collisions. Nucleons from different nuclei are considered to have collided if the distance between them in the transverse plane satisfies the condition:

$$d < \sqrt{\frac{\sigma_{NN}^{\text{inel}}}{\pi}}. \tag{5}$$

For a beam kinetic energy of $3.8A$ GeV, the adopted cross-section value is:

$$\sigma_{NN}^{\text{inel}} = 28.0 \text{ mb}. \tag{6}$$

In the two-component model, the number of particle sources is given by the expression:

$$\mathrm{N}_a(f) = fN_{\text{part}} + (1-f)N_{\text{coll}}. \tag{7}$$

The multiplicity distribution originating from these sources is described by a negative binomial distribution (NBD):

$$\begin{aligned} P_{\text{NBD}}(n;\mu,k,N_a) &= \frac{\Gamma(n+kN_a)}{\Gamma(n+1)\Gamma(kN_a)}\left(\frac{\mu}{\mu+k}\right)^n\left(\frac{k}{\mu+k}\right)^{n+kN_a}, \\ \frac{dN_{\text{model}}}{dn} &= N_0\sum_{i=1}^{N_{\text{events}}} P_{\text{NBD}}(n;\mu,k,N_{a,i}). \end{aligned} \tag{8}$$

The measured multiplicity $RefMult$ was linked to the collision geometry via the two-component particle production model and the negative binomial distribution. The number of ancestors $N_a(f)$ from Eq. (7) and the model distribution from Eq. (8) were utilized. The parameters varied during the fitting procedure included the parameter f, which determines the relative contribution of N_{part} and N_{coll}, the mean multiplicity μ per source, the fluctuation parameter k, and the normalization factor N_0. For each set of parameters, the model $RefMult$ distribution was constructed by summing the contributions from all MC-Glauber events and then

compared to the experimental data; the expected number of events was calculated by integrating the model function within the histogram bin boundaries. The fitting was performed over the multiplicity of tracks that satisfied the criteria detailed in Section 3.1, specifically within the region where the trigger and primary vertex reconstruction efficiencies are close to unity. Following the fit, the model distribution was divided into intervals corresponding to percentiles of the inelastic cross-section; for each centrality class, the distributions of b, N_{part}, and their mean values were extracted.

The result of the fit to the BM@N data for Xe + CsI at 3.8A GeV is shown in Fig. 11: open symbols represent the experimental $RefMult$ distribution, the blue line shows the MC-Glauber result, vertical lines indicate the boundaries of the centrality classes, and the bottom panel shows the ratio of the data to the calculation. The extracted parameters are $f = 1.0$, $\mu = 0.3$, $k = 500.0$, with an integrated efficiency of $\varepsilon_{\mathrm{int}} = 0.724$ and $\chi^2/\mathrm{ndf} = 0.95$. Within the adopted parameterization, $f = 1$ corresponds to a scaling of the number of sources with N_{part}, while a large value of k implies a minimal additional width for the NBD; these parameters are effective parameters and should not be interpreted as independent dynamic observables. The value of the test statistic indicates a satisfactory description of the distribution shape within the selected fitting region.

Table 1: Parameters of centrality intervals

Centrality, %	RefMult Range	$\langle b \rangle$, fm	RMS	$\langle N_{\mathrm{part}} \rangle$	RMS
0–10%	56–120	2.85	1.15	187.21	24.39
10–20%	40–56	4.88	0.93	136.78	23.61
20–30%	28–40	6.36	0.80	97.09	19.38
30–40%	19–28	7.55	0.77	67.07	15.70
40–50%	13–19	8.54	0.77	45.69	12.47
50–60%	8–13	9.45	0.82	29.69	10.08

3.3 Centrality estimation via direct reconstruction method

The method of direct impact parameter reconstruction was proposed in the works of Rogly, Giacalone, and Ollitrault, as well as Das and co-authors [23; 24]. Its core idea is to reconstruct the relationship between the measured event activity and

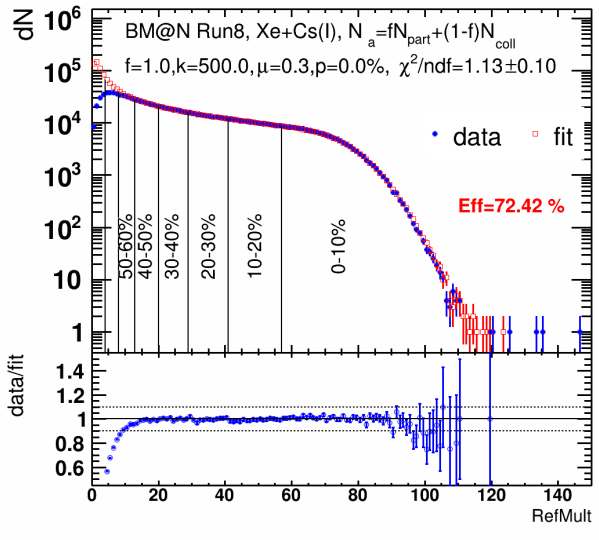

Figure 11: Fit to the charged particle multiplicity distribution in Xe + CsI collisions at a beam energy of 3.8A GeV using the MC-Glauber method. Closed symbols correspond to BM@N Run 8 data; the red line shows the result of the fit with the geometric calculation for the Xe + CsI system.

the collision geometry directly from the experimental distribution of an observable. In this analysis, the charged particle multiplicity (M_{ch}) is used as such an observable.

The centrality (c_b) is introduced, defined via the cumulative impact parameter distribution:

$$c_b = \int_0^b P(b')\, db', \tag{9}$$

such that $P(c_b) = 1$ and c_b is uniformly distributed in the interval from 0 to 1. The inclusive multiplicity distribution is written as:

$$P(M_{ch}) = \int_0^1 P(M_{ch} \mid c_b)\, dc_b, \tag{10}$$

where $P(M_{ch} \mid c_b)$ describes multiplicity fluctuations at a fixed collision geometry.

Since the multiplicity is non-negative, a gamma distribution is used as the fluctuation kernel:

$$P(M_{ch} \mid c_b) = \frac{M_{ch}^{k(c_b)-1} \exp[-M_{ch}/\theta]}{\Gamma[k(c_b)]\, \theta^{k(c_b)}}, \tag{11}$$

where $k(c_b)$ is the shape parameter, and θ is the scale parameter. The mean value

and variance are expressed through them as:

$$\langle M_{ch}(c_b)\rangle = \theta\, k(c_b), \qquad D(M_{ch} \mid c_b) = \theta^2\, k(c_b). \tag{12}$$

The experimental distribution $P(M_{ch})$ does not contain enough information to reconstruct the centrality dependencies of both the mean and the variance simultaneously. Therefore, following [23; 25], it is assumed that the reduced fluctuation θ is constant with respect to centrality, and only the shape parameter k depends on c_b. A monotonically decreasing parametrization is used for it:

$$k(c_b) = k_{\max}\,[1 - c_b^{\alpha}]^{\gamma} + k_{\min}, \tag{13}$$

which guarantees monotonicity and allows describing typical shapes of the observable's dependence on the impact parameter. The exponent α controls the presence of a plateau at small b (for $\alpha \geq 1$, the derivative $dk/db \to 0$ in the region of the most central collisions), γ determines the curvature of the dependence, and $k_{\min}$ sets a non-zero shift associated with the trigger threshold. The value of the observable in head-on collisions ($c_b = b = 0$) equals:

$$M_{ch}^{\max} = \langle M_{ch}(b=0)\rangle = \theta\,(k_{\max} + k_{\min}). \tag{14}$$

Thus, the free parameters for fitting the inclusive distribution are α, γ, θ, $k_{\min}$, and $k_{\max}$; once they are determined, the conditional kernel (11) is completely specified, and the geometry distribution for a given multiplicity is reconstructed using Bayes' theorem.

To transition from centrality c_b to the absolute impact parameter, it is necessary to define the shape of the inclusive distribution $P(b)$. For data selected with a minimum-bias trigger, it can be approximated [25] as:

$$P(b) = \frac{2\pi b}{1 + \exp\left(\dfrac{b - b_0}{\Delta b}\right)}, \tag{15}$$

where $\Delta b \approx 0.4$ fm, and the parameter b_0 is found from the measured total reaction

cross section σ_R by inverting the relation:

$$\sigma_R = -2\pi(\Delta b)^2 \,\mathrm{Li}_2\left[-\exp\left(\frac{b_0}{\Delta b}\right)\right], \tag{16}$$

where $\mathrm{Li}_2(z)$ is the dilogarithm. The corresponding relationship $c_b(b)$ is obtained by substituting (15) into (9).

Reconstructing trigger efficiency via the inverse Bayes method requires a physically justified constraint on the dependence of the mean multiplicity on the impact parameter. The parametrization of this dependence used in the INDRA method itself cannot describe events missing from the sample due to trigger inefficiency: their contribution cannot be reconstructed solely from the registered distribution. Numerical parametrizations obtained from heavy-ion collision models can serve as such a constraint. In this work, the dependence of the mean multiplicity on b, calculated within the DCM–QGSM–SMM model, was used to estimate the trigger efficiency. The resulting efficiency estimate was then taken into account jointly with an INDRA-like parametrization when fitting the multiplicity distribution.

The application of the method to the multiplicity distribution in $\mathrm{Xe} + \mathrm{CsI}$ collisions at a beam energy of $3.8A$ GeV is shown in Fig. 12. The fit yielded the values of α, γ, θ, $k_{\min}$, $k_{\max}$ shown in the figure, $\chi^2/\mathrm{ndf} = 1.35$, and an integrated efficiency of:

$$\varepsilon_{\mathrm{int}} = 0.728. \tag{17}$$

In the region of intermediate and large multiplicities, the function describes the experimental data well, while at small M_{ch}, the recorded number of events is lower than the reconstructed full distribution due to the finite efficiency of the trigger and primary vertex reconstruction; the onset of the discrepancy corresponds to the anchor point position determined by the MC-Glauber method. The obtained centrality intervals and their corresponding mean impact parameter values are presented in Table 2.

A comparison of the results obtained by the MC-Glauber method and the direct reconstruction method demonstrates good agreement for the multiplicity ($RefMult$) slicing for the 0–60% classes: the boundaries of the corresponding

intervals match, and the mean impact parameter values $\langle b \rangle$ agree within 0.1 fm.

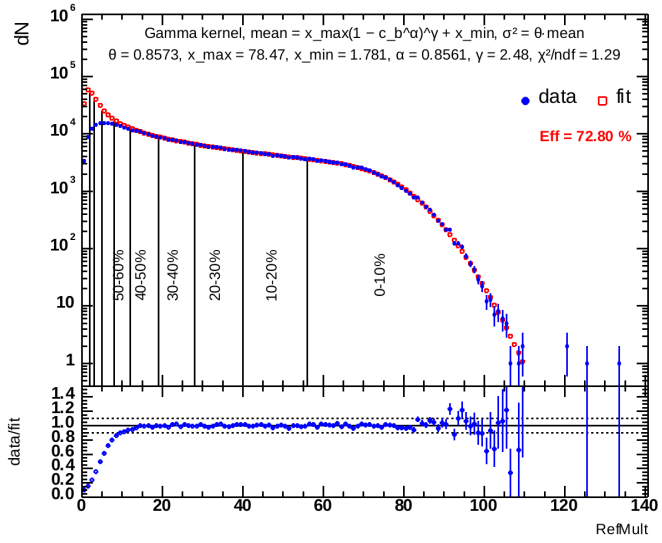

Figure 12: Fitting of the charged particle multiplicity distribution in Xe + CsI collisions at a beam energy of 3.8A GeV using the direct reconstruction method. Closed symbols correspond to BM@N Run 8 data, and the red curve represents the Γ-fit result.

Table 2: Centrality interval parameters based on the Γ-fit method results.

Centrality, %	RefMult range	$\langle b \rangle$, fm	RMS, fm
0–10%	56–120	2.83	1.12
10–20%	40–56	4.91	0.84
20–30%	28–40	6.38	0.70
30–40%	19–28	7.56	0.63
40–50%	12–19	8.63	0.62
50–60%	8–12	9.55	0.66

3.4 Run-by-Run Multiplicity Correction

During the eighth data-taking run of the BM@N experiment, variations in the working gas temperature and voltage in the tracking GEM detectors were observed. Since the gas gain and detection efficiency depend on these parameters, these changes led to fluctuations in the total number of detected tracks (N_{Tracks}) and modified their multiplicity distribution (RefMult).

An approach based on multiplicity correction by the distribution shape is proposed in this work. The procedure is as follows:

1. Selection of a stable reference period by RunId (8150-8200).

2. For each dataset with a specific RunId, the inflection point value of the refMult distribution in the high-multiplicity region is determined by fitting the tail of the distribution with the error function:

$$f(\text{refMult}) = A \cdot \text{Erf}\big(-\sigma \cdot (\text{refMult} - h)\big) + A, \tag{18}$$

   where:

   - A is the amplitude coefficient;
   - σ is the slope steepness parameter;
   - h is the position of the inflection point (the point to be determined).

3. The refMult values for each dataset with a specific RunId are corrected relative to the reference period 8150–8200 according to the following relations:

$$\text{RunId}_{\text{CorrFactor}} = \frac{1}{h}, \tag{19}$$

$$\text{refMult}_{\text{Corr}} = \text{refMult} \cdot \text{RunId}_{\text{CorrFactor}}. \tag{20}$$

Figure 13 shows the multiplicity distribution for each RunId before the correction procedure (left), the correction factor (center), and the result after correction (right).

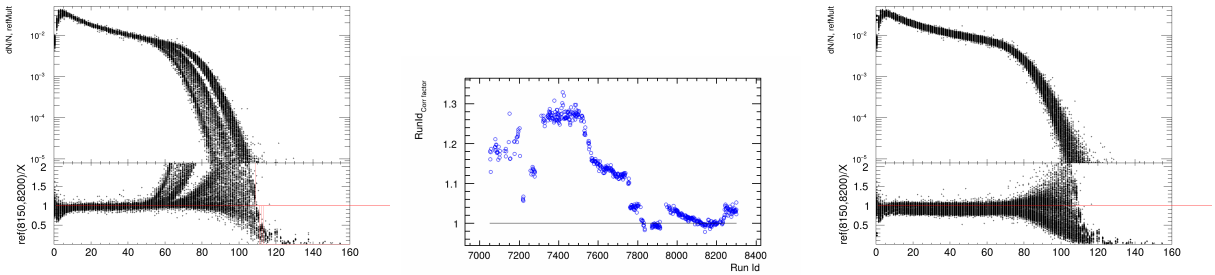

Figure 13: Multiplicity distribution for different RunIds before correction (left), correction factor (center), and the result after correction (right).

Figure 16 shows the proton p_T spectra for different centrality classes. Figure 17 shows the proton p_T spectra in six centrality intervals.

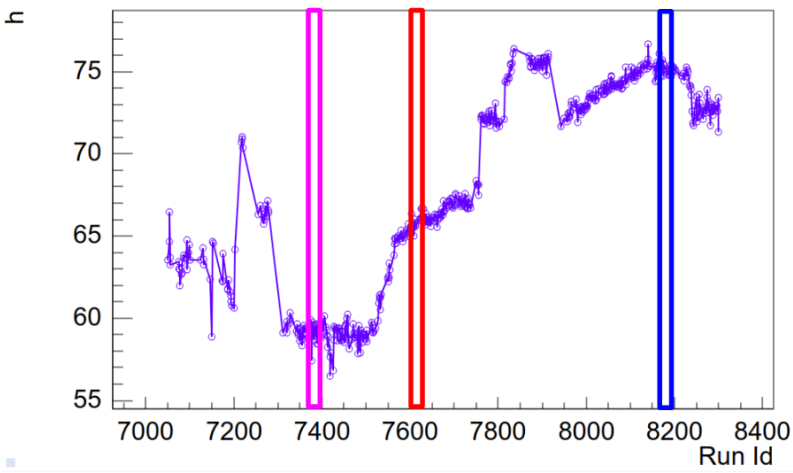

Figure 14: Dependence of the parameter h for multiplicity correction on the run number (RunId).

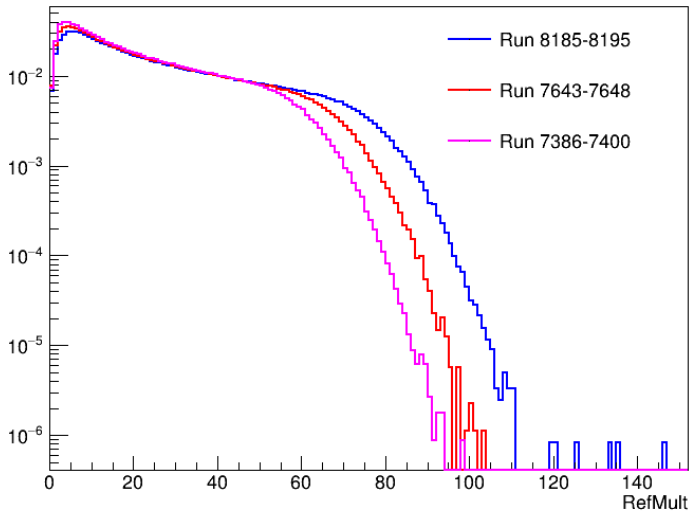

Figure 15: RefMult multiplicity distribution obtained in three different reference groups.

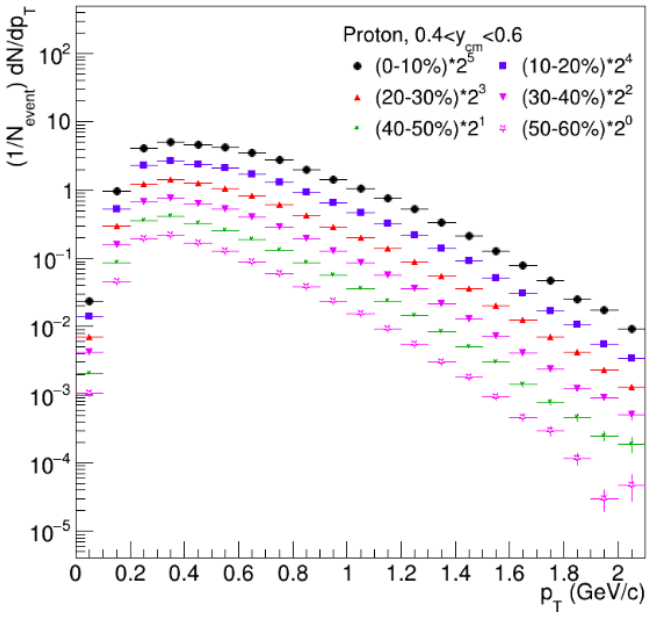

Figure 16: Proton p_T spectra for different bins in centrality.

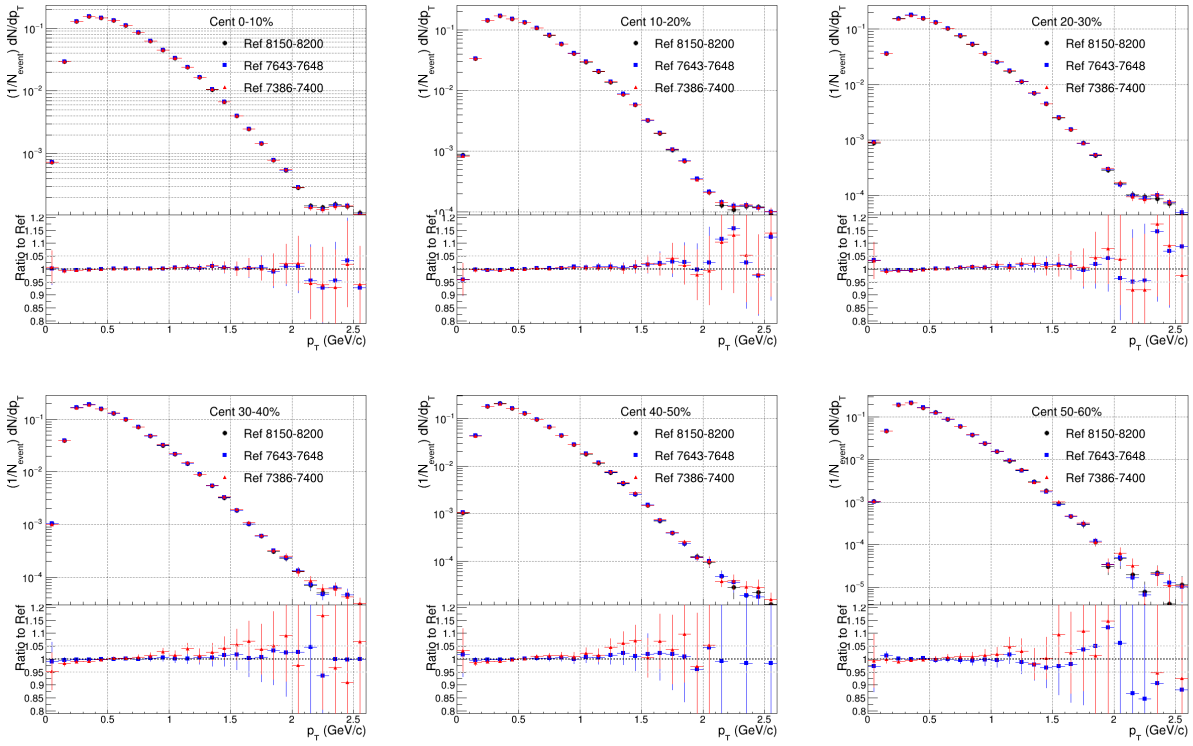

Figure 17: Proton p_T spectra in six centrality intervals. The centrality was determined in 3 different reference run groups.

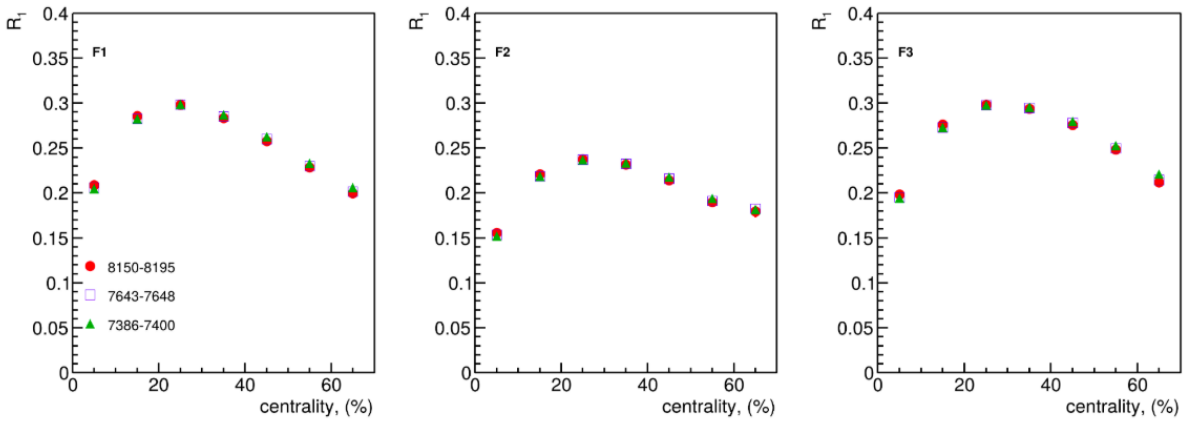

Figure 18: Resolution of symmetry planes F1, F2, F3, measured by the 3(4)-subevent method as a function of centrality. Results where centrality was determined in different reference run groups are shown with different colors and markers.

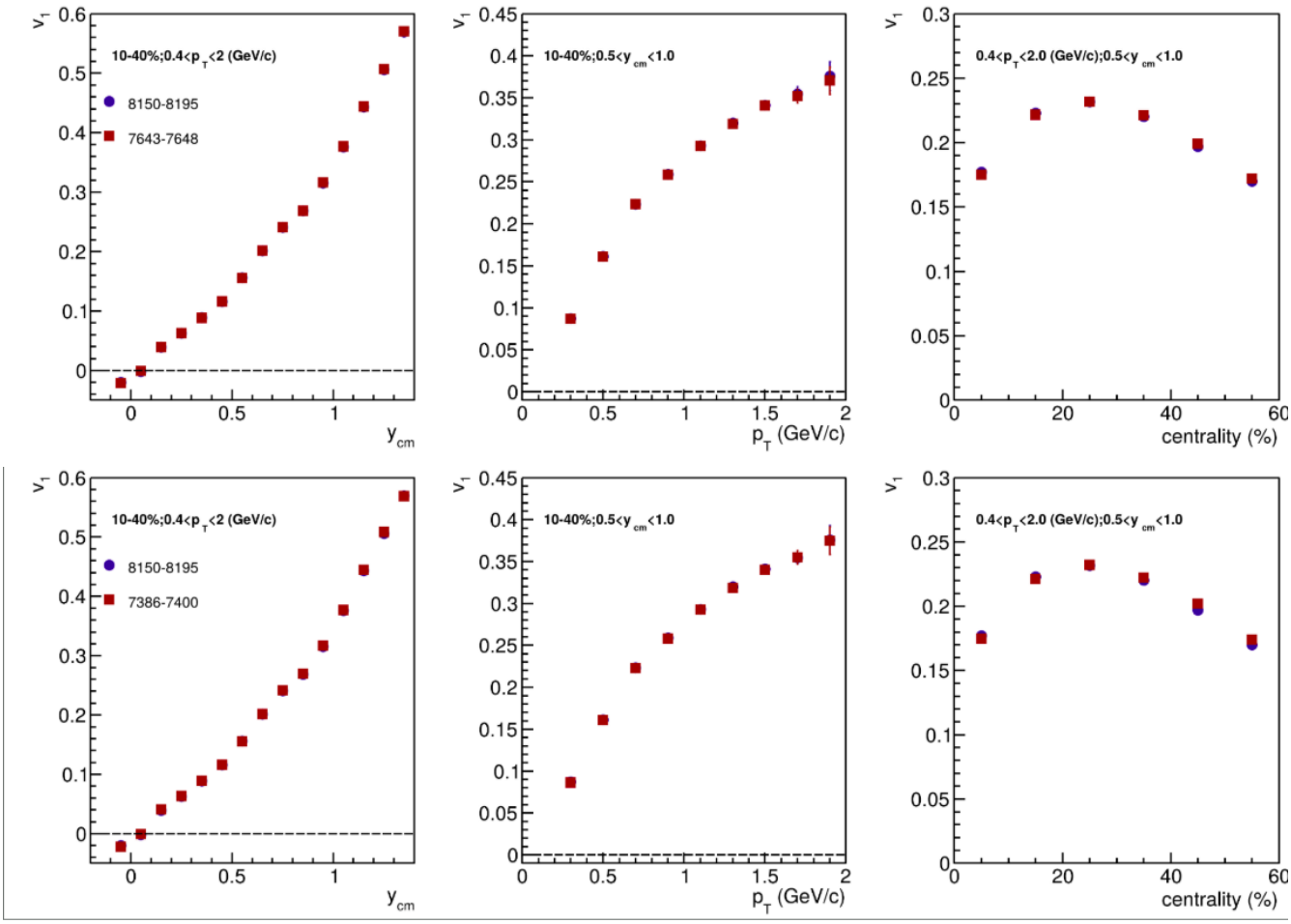

Figure 19: Dependence of the directed flow coefficient on centrality. Results where centrality was determined in different reference run groups are shown with different colors and markers.

3.5 Efficiency Evaluation

The trigger system efficiency was determined as a function of the number of tracks used to reconstruct the primary vertex, in accordance with the methodology described in [26]. The efficiency of the main trigger CCT is calculated as the product of the efficiencies of the multiplicity detector BD and the fragment detector FD:

$$\epsilon_{CCT} = \epsilon_{BD}\,\epsilon_{FD}. \tag{21}$$

Each of the quantities ϵ_{BD} and ϵ_{FD} is defined as the ratio of the number of events that passed the selections (primary vertex with ≥ 2 tracks, signal in the trigger window, $N_{BD} \geq 4$ for BD, and FD signal below the xenon threshold for FD) to the number of events selected by an independent trigger that does not include the detector under test (MBT for BD, CCT1 for FD):

$$\epsilon_{BD} = \frac{N(\mathrm{BD} \geq 4 \wedge \mathrm{MBT})}{N(\mathrm{MBT})}, \qquad \epsilon_{FD} = \frac{N(\mathrm{FD} \wedge \mathrm{CCT1})}{N(\mathrm{CCT1})}. \tag{22}$$

These quantities are plotted as functions of the number of tracks in the primary vertex N_{TrPV}, and then converted into the dependence of ϵ_{CCT} on the impact parameter b using the DCM-SMM model.

In addition to the described methodology, the selection criterion for suppressing event pile-up from multiple beam ions was improved. In Fig. 20 (right panel), the violet markers show the result without applying the improved selection, while the red markers show the result with its application. After introducing this criterion, the efficiency dependence on N_{TrPV} becomes consistent with the result obtained for events with a single xenon ion.

The methodology described above was applied not only as a function of the number of tracks in the primary vertex N_{TrPV}, but also as a function of RefMult: for each RefMult interval, the dependencies of ϵ_{BD}, ϵ_{FD}, and their product ϵ_{CCT} were constructed in a similar manner (black line in Fig. 21). An independent evaluation of the same dependence was obtained from the fitting of the multiplicity distribution using the direct reconstruction method (Sec. 3.3) and within the MC-Glauber framework (Sec. 3.2); these results are shown in Fig. 21 by blue and pink markers,

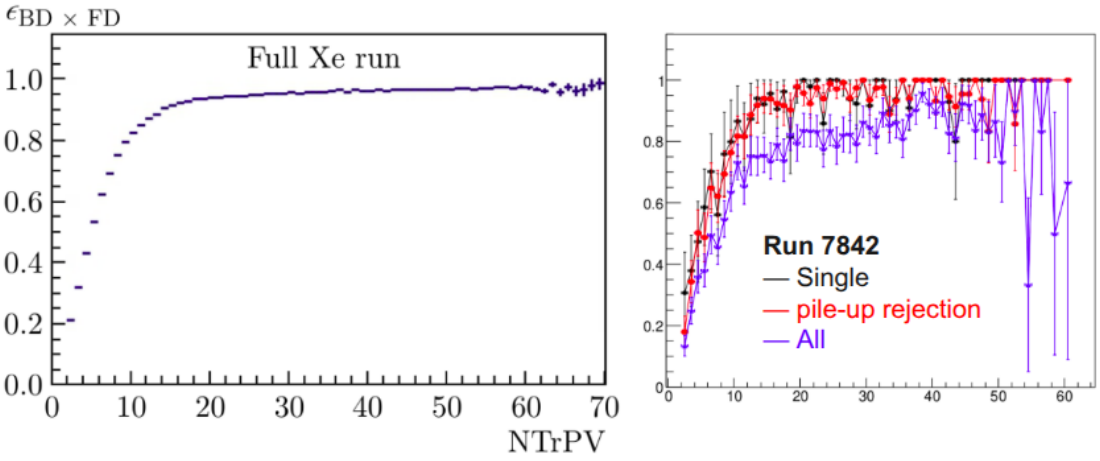

Figure 20: Comparison of efficiency as a function of the number of tracks in the primary vertex, obtained by the method described in the paper by V.A. Plotnikov (link) using the improved pile-up event selection.

respectively.

Additionally, a fourth evaluation was considered, utilizing data recorded with the beam trigger BT, which is close to a minimum-bias trigger (red markers in Fig. 21). In this approach, the main trigger efficiency was defined as the ratio of the number of events recorded with the CCT trigger to the number of events recorded with the BT trigger in each RefMult interval. Since the BT trigger does not include multiplicity conditions in the BD or signal conditions in the FD, this evaluation is independent of the efficiencies of these detectors and serves as an independent cross-check of the results obtained by the methodology described above.

A comparison of the four efficiency evaluations is presented in Fig. 21. The best agreement with the result obtained from the BT trigger data is demonstrated by the evaluations from the MC-Glauber and gamma-fit methods: across the entire considered RefMult region, they coincide with the CCT/BT ratio within uncertainties. All four methods agree with each other above the anchor point corresponding to RefMult $\approx$ 15; in this region, the efficiency reaches a plateau close to unity, which confirms the correctness of the trigger loss description when transitioning to more central collisions. Below the anchor point, the discrepancy between the methods increases, reflecting the growing relative contribution of trigger losses and the uncertainties in their modeling for peripheral events.

To validate the MC-Glauber method as an efficiency reconstruction tool, a test

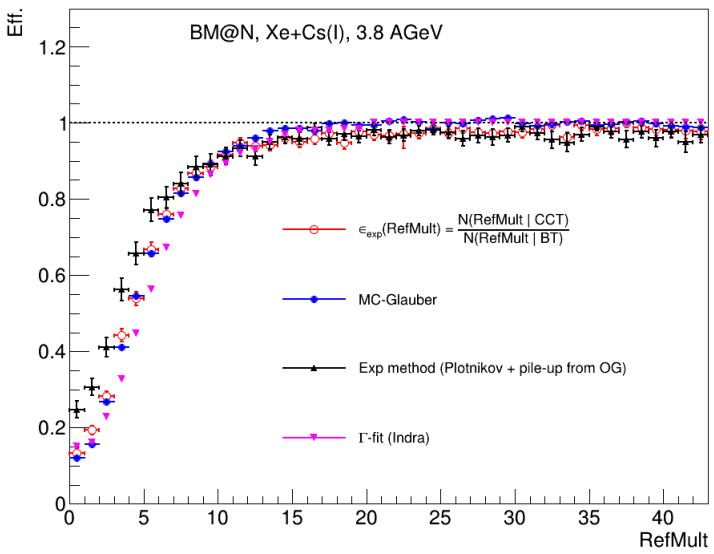

Figure 21: Efficiency as a function of RefMult obtained by different methods: black line — Plotnikov method with improved pile-up event selection, red line — efficiency obtained from BT run data, blue — from the MC-Glauber method, pink — from the direct reconstruction method (Γ-fit).

with controlled losses was performed. The CCT was used as the initial trigger, after which an offline selection was applied to the data, cutting off peripheral events by the condition $N_{BD} > 10$. The RefMult distributions for the initial and truncated samples are compared in Fig. 22, and the result of the refitting by the MC-Glauber method for the CCT($N_{BD} > 10$) conditions is shown in Fig. 23. The fraction of cut-off events under this selection is known independently and amounts to about 32%, so the expected integrated efficiency of the truncated sample is $\varepsilon \approx 0.72 \times (1 - 0.32) \approx 0.49$. Fitting the truncated sample yields an integrated efficiency of 48.96%, which is consistent with this expectation and confirms that the method reproduces the known loss. In addition to the integrated value, the method correctly describes the differential dependence of efficiency on RefMult (Fig. 24).

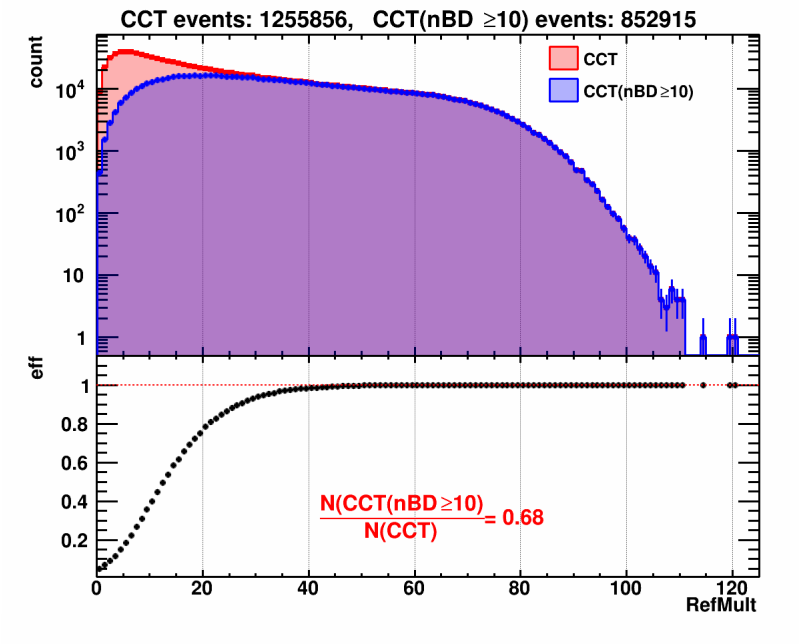

Figure 22: Comparison of RefMult distributions for CCT and CCT($n_{\mathrm{BD}} \geq 10$) conditions.

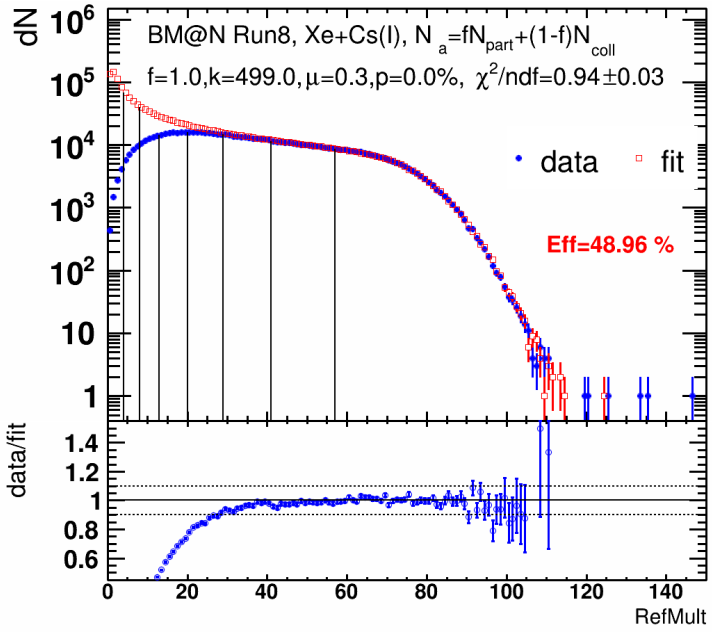

Figure 23: Approximation of the charged particle multiplicity distribution with the condition $n_{\mathrm{BD}} \geq 10$ in Xe + CsI collisions at a beam energy of 3.8A GeV using the MC-Glauber method. Closed symbols correspond to BM@N Run 8 data, red line represents the fitting result with a geometric calculation for the Xe + CsI system.

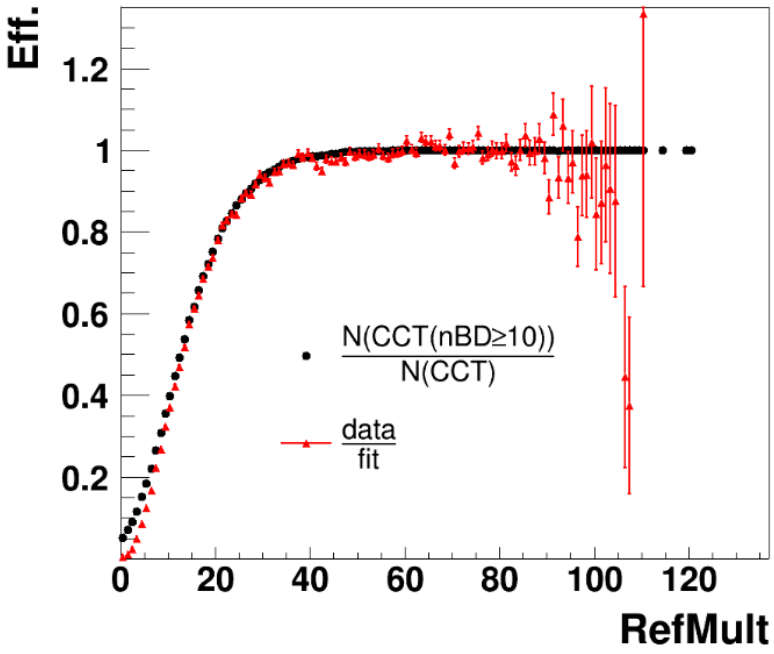

Figure 24: Event selection efficiency with the condition $n_{\mathrm{BD}} \geq 10$ as a function of RefMult.

3.6 Estimation of the Off-Target Collision Fraction

Off-target collisions can introduce distortions into the results of anisotropic flow measurements. An estimation of the fraction of such collisions was performed for the events selected for this analysis.

The event selection replicates the one used for measuring the anisotropic flows of protons (CCT2 trigger, VC counter signal below the threshold, absence of additional beam ions near the trigger time; at least two tracks were used for primary vertex reconstruction, the coordinates of the primary vertex along the x and z axes were within 3 standard deviations from the mean values in a given run, and along the y axis, less than 1.2 cm).

To estimate the fraction of off-target events, empty-target runs were used, which were periodically recorded throughout the data-taking period. To account for variations in the beam characteristics (Fig. 25), empty-target runs closest to the investigated ones were selected for the analysis.

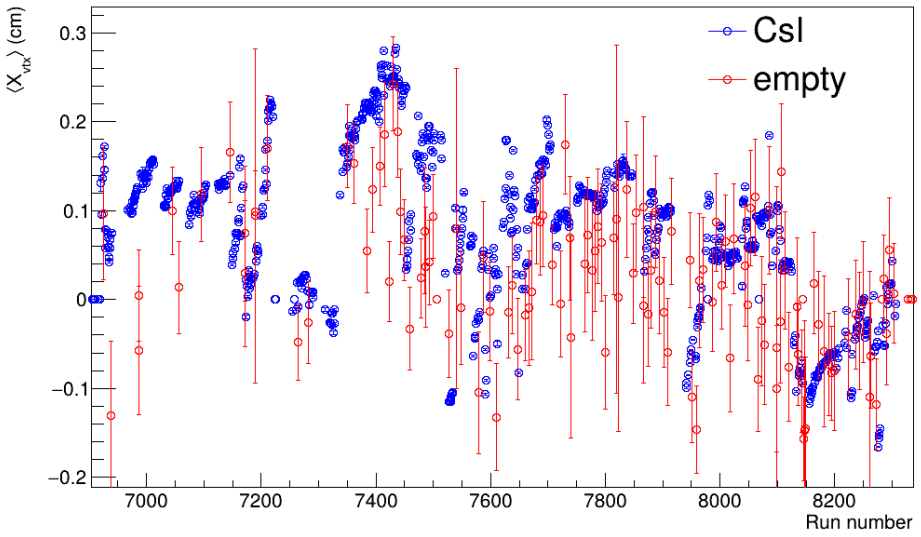

Figure 25: Mean position of reconstructed primary vertices along the x axis for runs with the CsI target (blue open symbols) and the empty target (red open symbols).

Figure 26 shows the distributions of the reconstructed vertices along the x and y coordinates for several empty-target runs. A characteristic crescent-shaped structure, caused by the beam hitting the target support frame (frame radius of 1.5 cm), does not change its position. Therefore, to exclude such collisions, it was

proposed to select events with vertex coordinates falling within a circle of 1.4 cm radius centered with a 0.2 cm shift along the y axis (Fig. 27). Depending on the run, this criterion rejects up to 4% of events (Fig. 28).

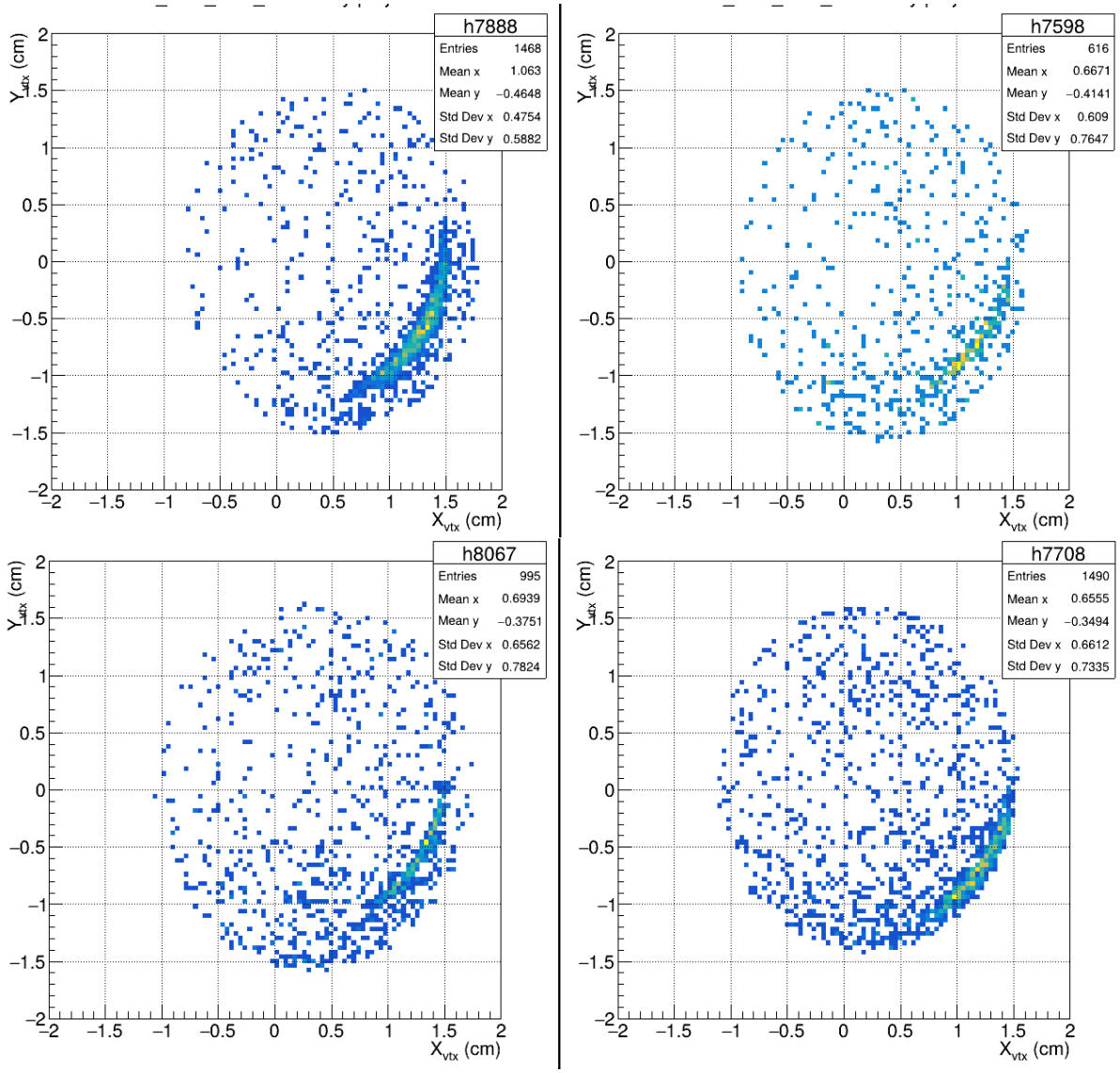

Figure 26: Distribution of reconstructed primary vertices along the x and y coordinates for several empty-target runs.

To estimate the fraction of off-target collisions, normalization of the number of events in the empty-target runs is required. During the data-taking period, two empty-target runs were recorded with the beam trigger (BT), allowing this normalization to be obtained directly. For runs with a mixed trigger, it is proposed to perform normalization to the number of collisions on the materials of the beam detectors located upstream of the target. Figure 29 shows the distributions of re-

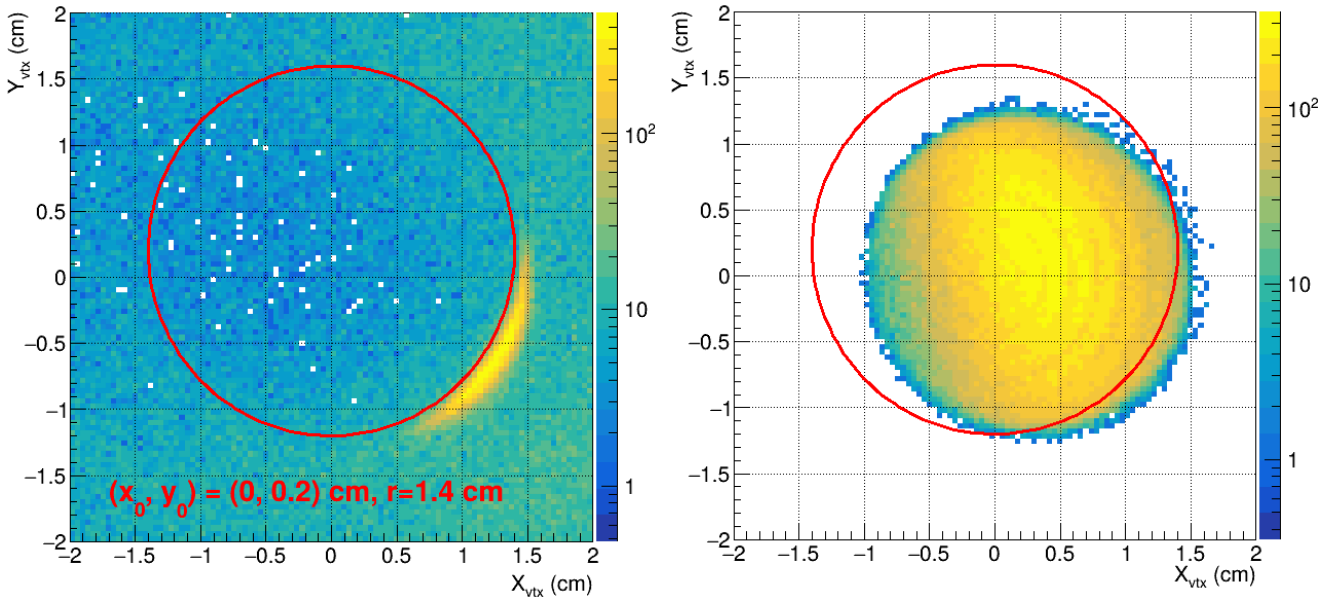

Figure 27: Selection of reconstructed primary vertices by x and y coordinates for the sum of empty-target runs (left) and for run 8066 (right).

constructed primary vertices along the z coordinate for events satisfying the above selection criteria for runs with the BT trigger (8281–8283). The number of events in empty-target runs is normalized to the number of BT triggers before the vertex coordinate selection. The distributions clearly exhibit peaks that are close in position and shape in the regions of $z = -104$ cm, $z = -84$ cm, and $z = 0$ cm, which correspond to the positions of the third station of the Silicon Beam Tracker (SiBT3), the BC2 beam counter, and the target [**Afanasiev:2023opv**]. Normalization to the integral of these distributions in the range from -140 to -40 cm matches the normalization to the number of BT trigger counts within 4%.

Figure 30 shows the event distributions along the z coordinate of the reconstructed vertex for runs with a mixed trigger (8066–8067), normalized to the integral in the range from -140 to -40 cm. A clear agreement between the peaks corresponding to the beam counters can be observed. Figure 31 shows the same distributions on an enlarged scale in the vertex region. The fraction of off-target events was estimated as the ratio of the integrals of these distributions within three standard deviations from the mean vertex position for each run.

Figure 32 shows the distributions of the selected track multiplicity per event and the collision centrality determined from this multiplicity for mixed-trigger runs

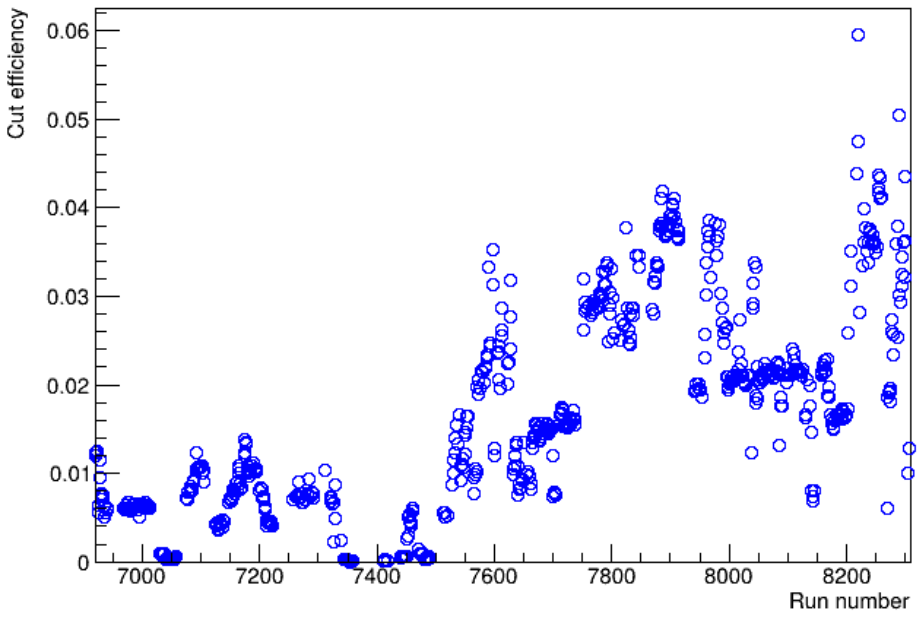

Figure 28: Fraction of events that do not satisfy the additional selection criterion for the primary vertex coordinates across different runs.

8066–8067, normalized to the number of collisions on the beam counters. It can be seen that off-target events constitute only a small fraction of peripheral collisions, reaching 1% only at centralities above 70%. Figure 33 shows the dependence of the off-target collision fraction on the run number for different centrality classes. For most runs at centralities below 60%, this value is less than 0.01%.

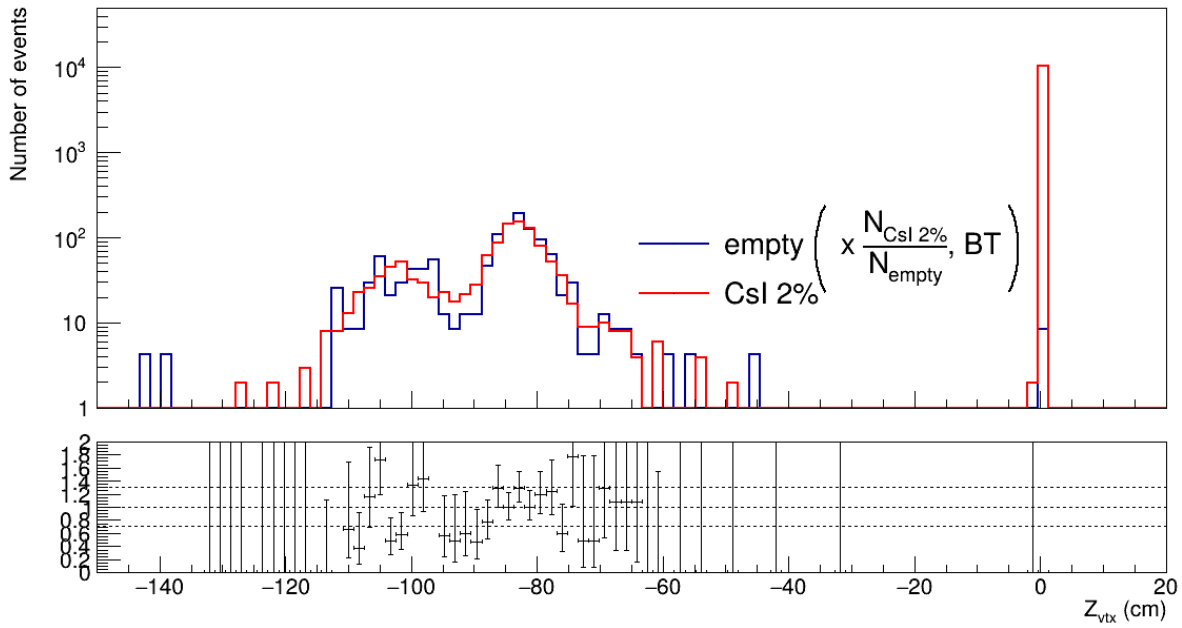

Figure 29: Event distributions along the z coordinate of the reconstructed vertex for runs with the BT trigger (8281–8283). Normalization to the number of triggers before vertex coordinate selection.

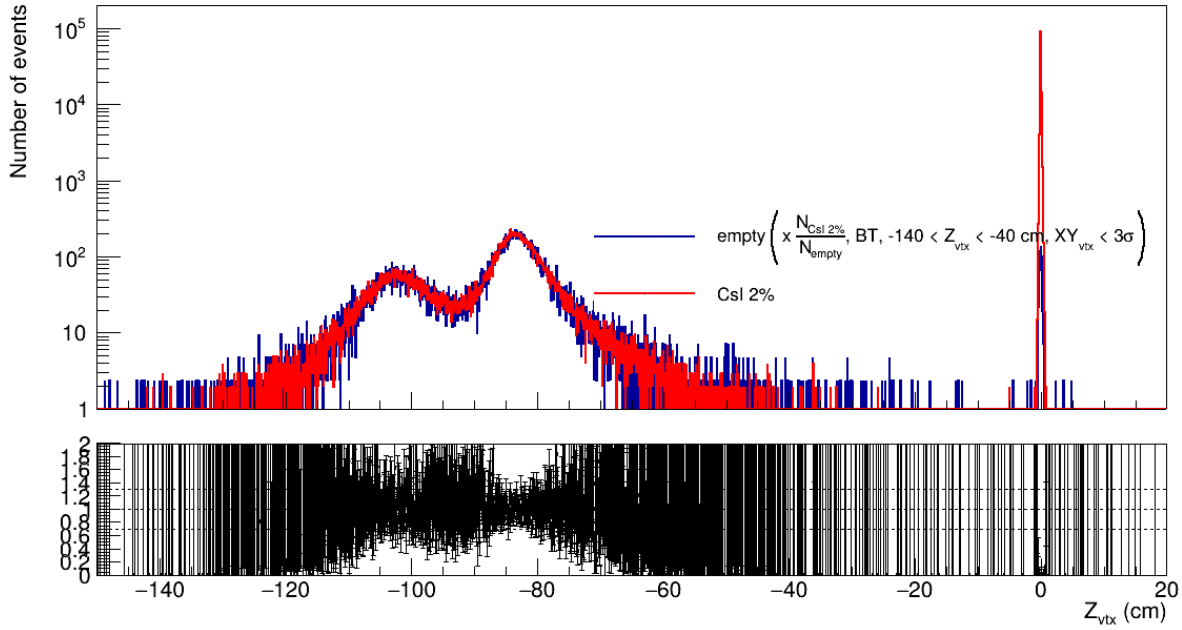

Figure 30: Event distributions along the z coordinate of the reconstructed vertex for runs with a mixed trigger (8066–8067). Normalization to the distribution integral in the range from -140 to -40 cm.

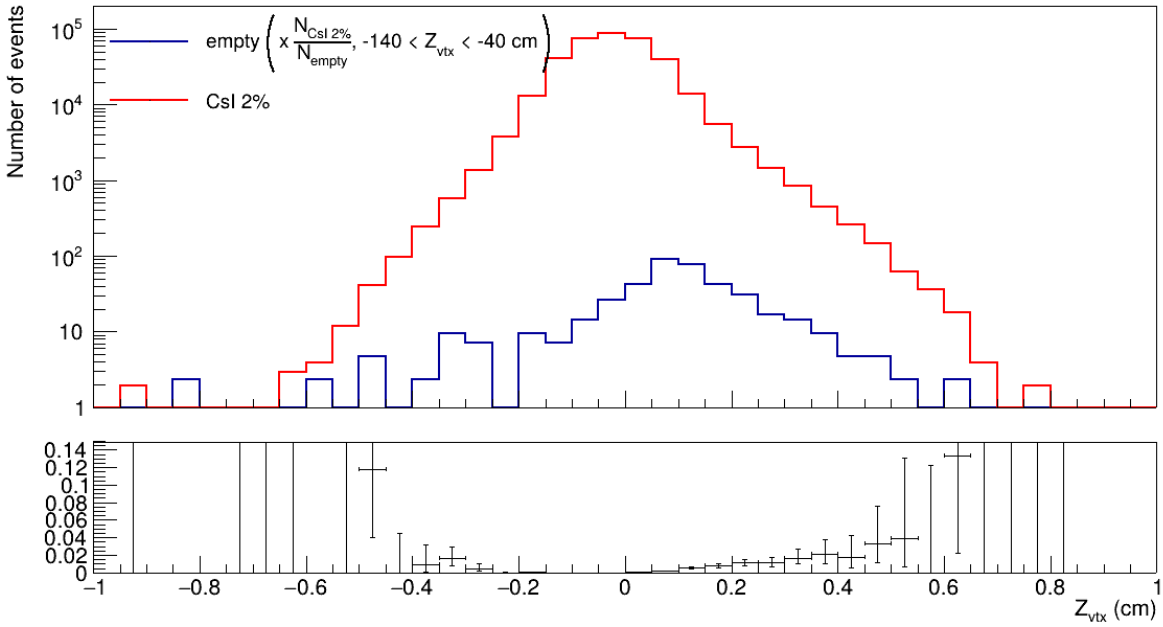

Figure 31: Event distributions along the z coordinate of the reconstructed vertex for runs with a mixed trigger (8066–8067) in the $z = 0$ region. Normalization to the distribution integral in the range from -140 to -40 cm.

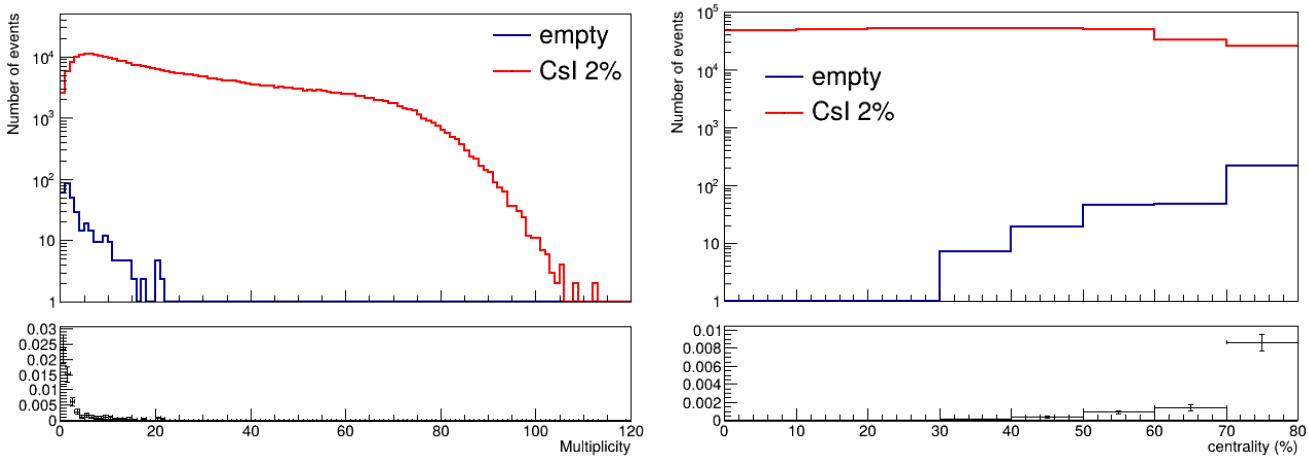

Figure 32: Distributions of selected track multiplicity per event (left) and collision centrality (right) for runs with a mixed trigger 8066–8067. Normalization to the number of collisions on the beam counters.

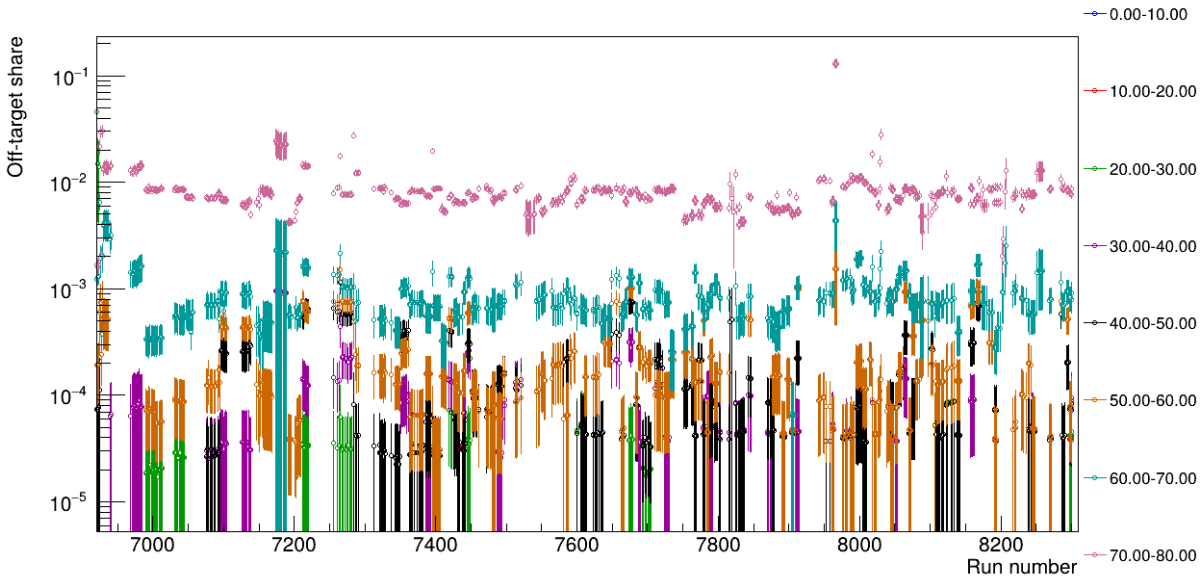

Figure 33: Dependence of the off-target collision fraction on the run number for different centrality classes.

4 Methods for analyzing anisotropic flow in BM@N

4.1 General framework for the flow measurements

We start from the brief description of the general framework for the measurements of flow coefficients v_n in the fixed target experiment [3–6; 18]. The observables for v_n coefficients can be written in terms of flow Q_n and unit u_n vectors [5; 6; 18]. For each particle k in the event the unit $u_{n,k}$ vector in the transverse (x,y) plane can be defined as:

$$u_{n,k} = e^{in\phi_k} = x_{n,k} + iy_{n,k} = \cos n\phi_k + i \sin n\phi_k, \tag{23}$$

where ϕ_k is the azimuthal angle of the particle's momentum. A two dimensional symmetry-plane (flow) Q_n-vector in the transverse plane is defined as a sum of unit $u_{n,k}$-vectors over a group of particles in the event:

$$Q_n = \frac{\sum_{k=1}^{M} w_k u_{n,k}}{\sum_{k=1}^{M} w_k} = X_n + iY_n = |Q_n| e^{in\Psi_n^E}, \tag{24}$$

where M is the multiplicity of particles in the selected group, Ψ_n^E is the symmetry plane angle of n-th harmonic and w_k is the weight of particle, which is used either to correct the azimuthal anisotropy of the detector or to account for the multiplicity of particles falling into a specific cell of a segmented detector [5; 6; 18].
Detectors are not required to measure individual particles to be able to reconstruct the symmetry plane. As long as the detector is sensitive to the shape of the particle distribution in the transverse plane, the symmetry-plane (flow) Q_n vector can be determined. For the case of a segmented detector, such as a calorimeter, the mean position of the individual channels correspond to $u_{n,k}$. The channel amplitudes correspond to the weights w_k assigned to the $u_{n,k}$ in Eq. 24. A segmented detector needs a segmentation which is larger than $2n$ to be able to measure the Q_n vector of harmonic n.

At very large multiplicities in the selected group ($M \to \infty$) sum can be sub-

stituted by the integral and equation 24 can be transformed as follows:

$$\lim_{M\to\infty} Q_n = \frac{\int_{2\pi} d\phi w(\phi) e^{in\phi} \rho(\phi - \Psi_n^R)}{\int_{2\pi} d\phi w(\phi) e^{in\phi} \rho(\phi - \Psi_n^R)} = \frac{\int_{2\pi} d\phi w(\phi) e^{in\phi - \Psi_n^R} e^{in\Psi_n^R} \rho(\phi - \Psi_n^R)}{\int_{2\pi} d\phi w(\phi) e^{in\phi} \rho(\phi - \Psi_n^R)} = V_n e^{in\Psi_R}, \quad (25)$$

where $V_n \propto v_n M$. From the equation above we can conclude that in limit of summation over very large group of particles in a event, $\Psi_n^E \to \Psi_n^R$ and Ψ_n^E is the estimation of reaction plane orientation in the event. We will refer to this estimation as symmetry plane of the collision or event plane of the collision.
Measurements of the azimuthal flow can be carried out projecting the u_n vector of selected particles onto symmetry plane of the collision (Scalar Product method):

$$v_n^{obs} = \frac{1}{2\pi}\langle u_n Q_n^* \rangle = \int d\Psi_n^R \int d\phi e^{in\phi} e^{-in\Psi_n^E} \rho(\phi - \Psi_n^R) = \langle \cos n(\phi - \Psi_n^R) V_n \cos n(\Psi_n^E - \Psi_n^R) \rangle. \quad (26)$$

Since the number of particles used for symmetry plane estimation is always limited, the cosine term with difference of symmetry plane angle and reaction plane angle will always be less than 1. Therefore correction R_n on the symmetry plane resolution is needed. This correction is provided using the resolution correction coefficient R_n defined as follows:

$$R_n = \langle V_n \cos n(\Psi_n^E - \Psi_n^R) \rangle. \quad (27)$$

Then the unbiased observable for the azimuthal flow of particles is defined by following equation:

$$v_n = \frac{v_n^{obs}}{R_n} = \frac{\langle u_n Q_n^* \rangle}{R_n}. \quad (28)$$

Since the reaction plane of the collision is unknown, calculation of the resolution correction factor R_n can be performed using the pairwise correlations of Q_n

vectors:

$$\langle Q_n^a Q_n^b * \rangle = \langle V_n^a \cos n(\Psi_n^a - \Psi_R) V_n^b \cos n(\Psi_n^a - \Psi_R) \rangle, \tag{29}$$

where a and b indices indicate two groups of particles in each of which the symmetry plane $\Psi_n^{a,b}$ estimation was carried out separately. In this work the resolution correction factor was calculated using the method of three sub-events. Using three groups of particles, say a, b and c, we can estimate resolution via this formula:

$$R_n\{a(b,c)\} = \sqrt{\frac{\langle Q_n^a Q_n^b \rangle \langle Q_n^a Q_n^c \rangle}{\langle Q_n^b Q_n^c \rangle}} \tag{30}$$

To suppress the correlations not correspondent to the initial collective motion of the produced particles (non-flow) we suggest defining a group of particles with sufficient (pseudo-) rapidity separation between each of symmetry planes a, b and c. In the case where this separation cannot be achieved (for example a and b or a and c are not separated) we can introduce additional symmetry plane vector d, and require (pseudo-) rapidity separation only between three of the event planes, say a and d, b and d, c and d and c and d. Slight modification of the three sub-event method produces the estimation of resolution correction factor produces which we going to call the method of four sub-events:

$$R_n\{a(d)(b,c)\} = \langle Q_n^a Q_n^d \rangle \sqrt{\frac{\langle Q_n^d Q_n^b \rangle \langle Q_n^d Q_n^c \rangle}{\langle Q_n^b Q_n^c \rangle}} \tag{31}$$

In this work we use the symmetry plane defined from the spectator energy deposition in a modular detector FHCal. In this case the first-order symmetry plane Q_1 can be estimated using the modification of formula 24:

$$Q_1 = \sum_{k=1}^{N} E_k e^{i\varphi_k} / \sum_{k=1}^{N} E_k, \tag{32}$$

where φ is the azimuthal angle of the k-th FHCal module, E_k is the signal amplitude seen by the k-th FHCal module, which is proportional to the energy of spectator. N denotes the number of modules in the group. To suppress the auto-correlations

between u_n and Q_n vectors we rejected protons with projected position in FHCal plane within the acceptance of FHCal.

Since the reaction plane orientation is random and uniform, in the case of the ideal detector acceptance, correlation of vectors can be substituted with the correlation of their components (for more details see [4; 5; 18]):

$$\langle Q_n^a Q_n^b \rangle = 2\langle X_n^a X_n^b \rangle = 2\langle Y_n^a Y_n^b \rangle, \tag{33}$$

or similarly for the three-particles correlation:

$$\langle Q_{2n}^a Q_n^b Q_n^c \rangle = 4\langle X_{2n}^a X_n^b X_n^c \rangle = 4\langle X_{2n}^a Y_n^b Y_n^c \rangle = 4\langle Y_{2n}^a X_n^b Y_n^c \rangle = -4\langle Y_{2n}^a Y_n^b X_n^c \rangle. \tag{34}$$

Based on this, one can use only correlations of components of Q_n and u_n vectors to calculate flow coefficients.

$$v_n = 2\frac{\langle x_n X_n^* \rangle}{R_n^x} = 2\frac{\langle y_n Y_n^* \rangle}{R_n^y}, \tag{35}$$

where $R_n^{x,y}$ notate values of resolution correction coefficient calculated using the X and Y components of Q_n-vectors.

For instance, equation 35 for v_1 can be rewritten as follows:

$$v_1 = \frac{2\langle y_1 Y_1^a \rangle}{R_1^y\{a\}}, \tag{36}$$

where y_1 and Y_1^a are y-components of u_1 and Q_1^a vectors respectively, and $R_1^y\{a\}$ is the resolution correction factor for Y_1^a:

$$R_1^y\{a(b,c)\} = \sqrt{\frac{2\langle Y_1^b Y_1^c \rangle}{2\langle Y_1^a Y_1^b \rangle 2\langle Y_1^a Y_1^c \rangle}}, \tag{37}$$

In case of an ideal detector, the Q_n-vector relation to the symmetry plane is limited only by the multiplicity of the particles within the acceptance. In reality,

the detector non-uniformity in ϕ and effects from the magnetic field, additional material etc., can bias the flow measurements. This leads to equations 33 and 34 are being no longer valid. Detector non-uniformities can be treated on the level of the flow Q_n vectors. The following procedure was introduced in [5]. The advantages compared to re-weighting of the azimuthal particle spectra is that the procedure also works with detectors that have holes in the azimuthal acceptance. The necessary correction factors can be fully determined from the data itself. Monte Carlo simulations are not needed. The corrections (re-centering, twist and rescaling) can also be generalized to a generic normalized flow vector q_n with the components x_n and y_n. Schematic representation of these corrections are shown in Figure 34.

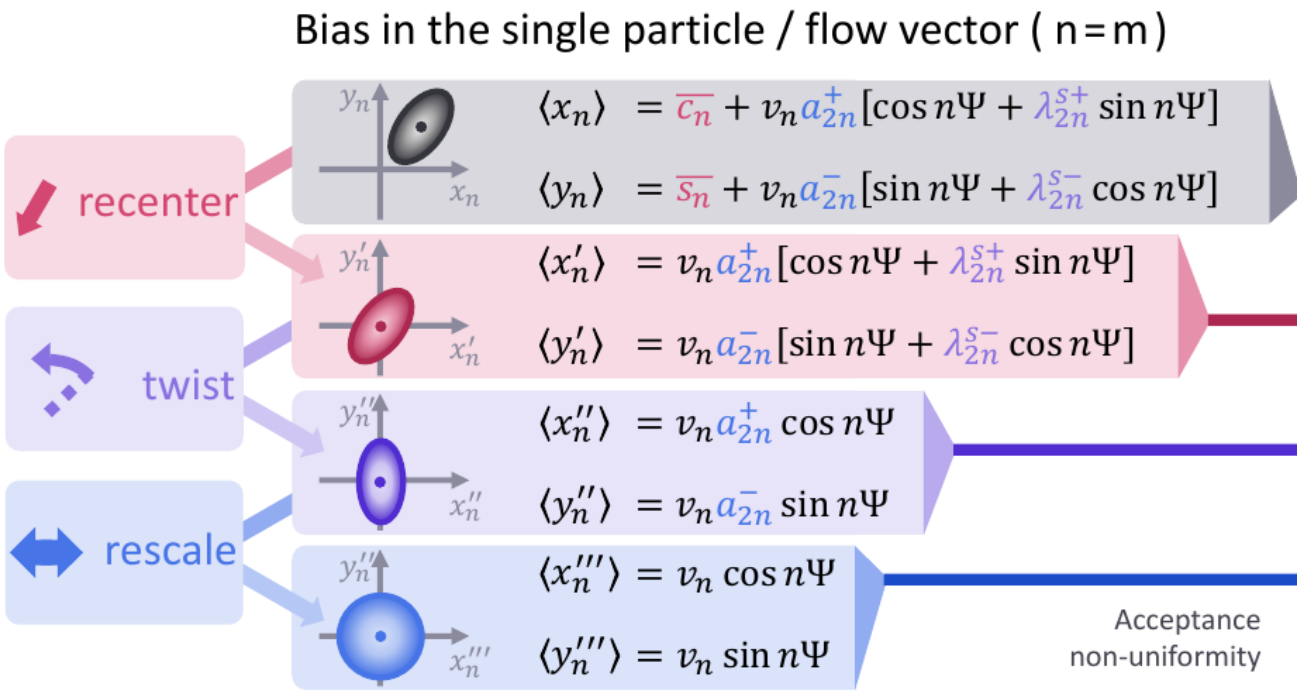

Figure 34: Schematic illustration of recentering, twist and rescale correction steps for q_n-vector introduced in [5].

Re-centering: A static shift of the detector signals can manifest in a shift of the average flow vector away from the origin. This shift can be removed by subtracting the mean flow vector from the flow vector in each collision.

Twist/Diagonalization: The flow vector distribution can appear twisted, if $sin(n\Psi)$, or $cos(n\Psi)$ terms bias the x_n and y_n components of the flow vectors. The

diagonalization corrections are calculated from the averaged flow vector components and applied to the flow vector in each collision.

Rescaling: A squashed flow vector distribution, which corresponds to different widths in the x and y direction, can be corrected with the rescaling correction.

The formalism of these corrections has been implemented in a software framework known as QnTools[27], which allows to perform the corrections of differential flow vectors, which may depend on a number of particle properties $q_n(p_T, \eta, PID, ...)$, see Figure 35.

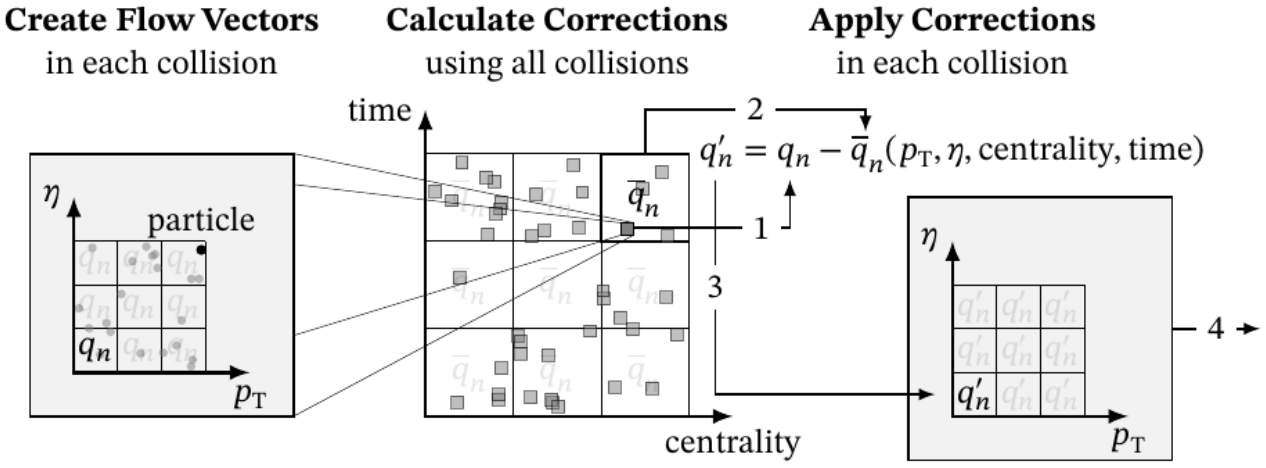

Figure 35: Sketch of the multi-dimensional correction procedure in the QnTools framework. As an example the recentering correction as a function of p_T, η, centrality, and time is shown.

4.2 The analysis of v_1 of protons from BM@N run8 data

In this subsection, we discuss the details of analysis of directed flow v_1 of protons in Xe+Cs(I) collisions at 3.8 AGeV using the BM@N run8 data.

1) To address the effects of the non-uniform acceptance we applied the corrections for both u_1 and Q_1 vectors :recentering, twist and rescaling. The QnTools framework [27] was used for corrections of u_1 and Q_1 vectors and flow analysis. For u_1-vector corrections were employed multi-differentially on transverse p_T, rapidity y and centrality. For the Q_1-vectors corrections were applied only differentially on centrality.

2) The detailed performance study, persented in the previus subsection, shows that due to magnetic field acting along the y-axis and deflecting charged particles along the x axis, we can measure the directed flow v_1 of protons using only the y components of flow vectors:

$$v_1 = 2\frac{\langle y_1 Y_1^a * \rangle}{R_1^y\{a\}}, \tag{38}$$

where the resolution correction factor is calculated using the method of three sub-events:

$$R_1^y\{a(b,c)\} = \sqrt{\frac{\langle Y_1^a Y_1^b \rangle \langle Y_1^a Y_1^c \rangle}{\langle Y_1^b Y_1^c \rangle}}, \tag{39}$$

or by the four sub-event method:

$$R_1^y\{a(d)(b,c)\} = \langle Y_1^a Y_1^d \rangle \sqrt{\frac{\langle Y_1^d Y_1^b \rangle \langle Y_1^d Y_1^c \rangle}{\langle Y_1^b Y_1^c \rangle}}, \tag{40}$$

3) The Q_1 vectors for symmetry planes in the FHCal have been obtained using the Eq. 32. Modules of the FHCal were divided into three groups (sub-events): F1, F2, F3 as it is shown in the Figure. 36. According to the simulations, due to charge splitting in the dipole analyzing magnet SP-41, F1 sub-event primarily registers the spectator protons, F2 — spectator fragments and F3 — neutrons, see the left part of Figure. 36.

Two additional sub-events were introduced from the tracks of the charged particles in the inner tracking system of BM@N. All negatively charged particles with pseudorapidity $1.5 < \eta < 3$ and transverse momentum $p_T > 0.2$ GeV/c comprise the

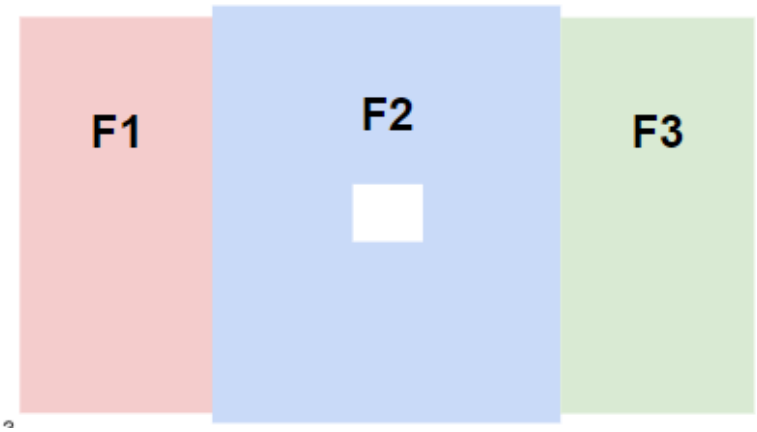

Figure 36: Layout of the FHCal modules division into three groups (sub-events): F1, F2, F3.

T- sub-event. The T+ sub-event consists of positively charged particles in following kinematic region: $2 < \eta < 3$ and $p_T > 0.2$ GeV/c.

Resolution correction factor was calculated for 3 spectator symmetry planes F1, F2, and F3 using the three sub-event method (for F2 four sub-event technique was employed as well) using the Equation 39 (and for four sub-events Equation 40). Figure 37 shows the centrality dependence of the resolution correction factors R_1 for sub-event symmetry planes F1, F2 and F3 from left to right. For each symmetry plane R_1 was estimated using 3 combinations of sub-events (as indicated in the figure). One can observe that all three estimations for each symmetry plane are in reasonable agreement. may suggests that the final values of R_1 resolution factors This fact may suggest that the contribution of non-flow correlations in the final values of R_1 is very small.

4) Figure 38 shows the centrality dependence of directed flow v_1 of protons in Xe+Cs(I) collisions at 3.8 A GeV. The measurements have been performed with respect to the F1, F2, F3 symmetry planes. The resulting v_1 values of protons are in a good agreement for the measurements with respect to F1, F2, F3 symmetry planes. The small difference in resulting v_1 values was used as an systematic error. In order to get the final results, the measurements of directed flow v_1 have been performed with respect to the combined (F1+F2+F3) symmetry plane, see Figure 39.

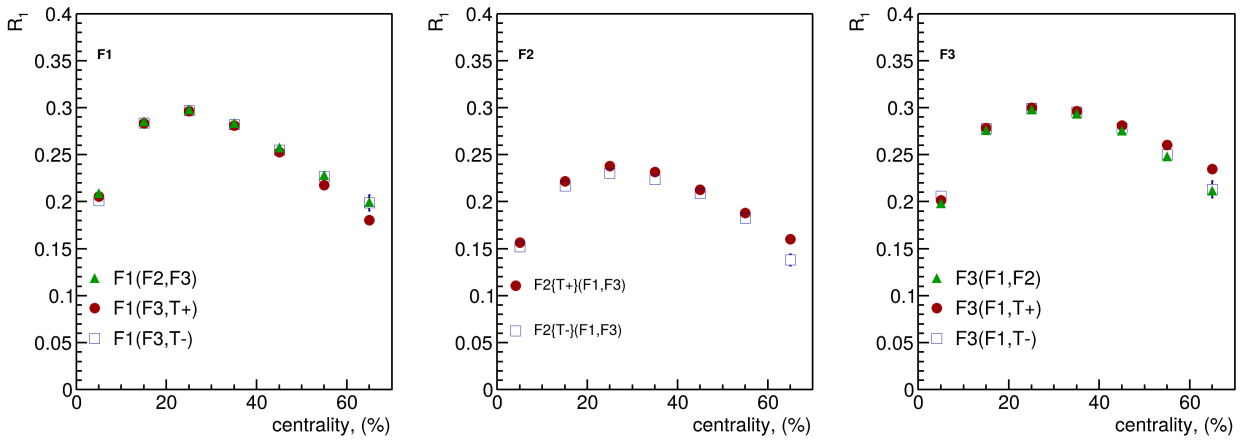

Figure 37: Resolution correction factor R_1 calculated using different combinations as a function of centrality for sub-event symmetry planes F1, F2 and F3 from left to right.

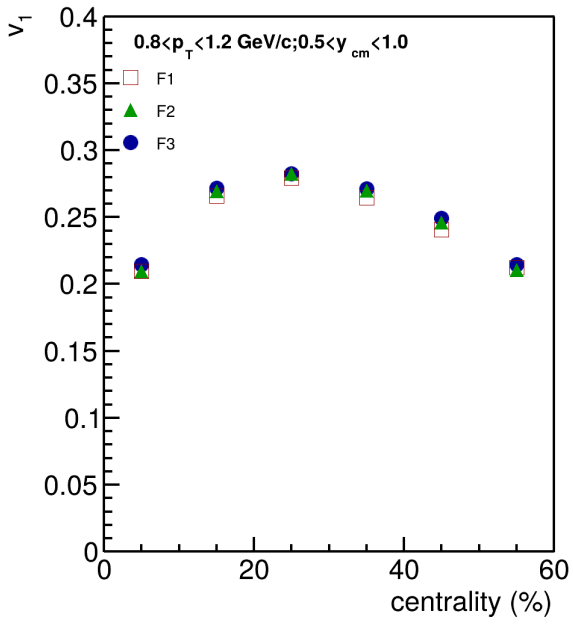

Figure 38: Directed flow v_1 of protons as a function of centrality measured with respect to different spectator symmetry planes: F1, F2, F3 , see text for the details.

4.3 Systematic uncertainties of v_1 measurements

In order to estimate systematic uncertainties of v_1 measurements , the following sources were considered:

- Uncertainty in proton momentum reconstruction. We varied the number of stations N_{hits} in inner tracking system used for track reconstruction as well as the values of track χ^2/NDF quality. The overall systematic uncertainty is found to be bellow 2-5%.

- Contribution from the secondary particles. We studied the difference in v_1 results for tracks with different Distance of the Closes Approach (DCA) to the primary vertex. It is found that proton v_1 values obtained with different DCA cut are in agreement within 1-2%.

- Contamination from the different particle species. We varied the identification selection criteria for protons. Observed is the systematic uncertainty is bellow 2-4%

- Acceptance and efficiency. We preform the v_1 flow measurements for protons detected in TOF-400 and TOF-700 separately. We perform the measurements with and without the applying the efficiency correction for protons based on MC simulations for run8. The results are in a good agreement and we can conclude that the mean value of transverse momentum p_T is not shifted in this rapidity range.

- Run-by-run systematics was estimated dividing the events into several run periods and comparing the results in each group. The systematic uncertainty is less than 5% and found to be less than statistical.

Systematic uncertainties were calculatad by the square root of quadratic sum of uncertainties from each source.

5 Results of the directed flow measurements

Directed flow v_1 of protons was measured in Xe+Cs(I) collisions at 3.8 AGeV as a function of centrality for selected bins in transverse momentum (p_T) and rapidity (y_{cm}), see Figure. 39.

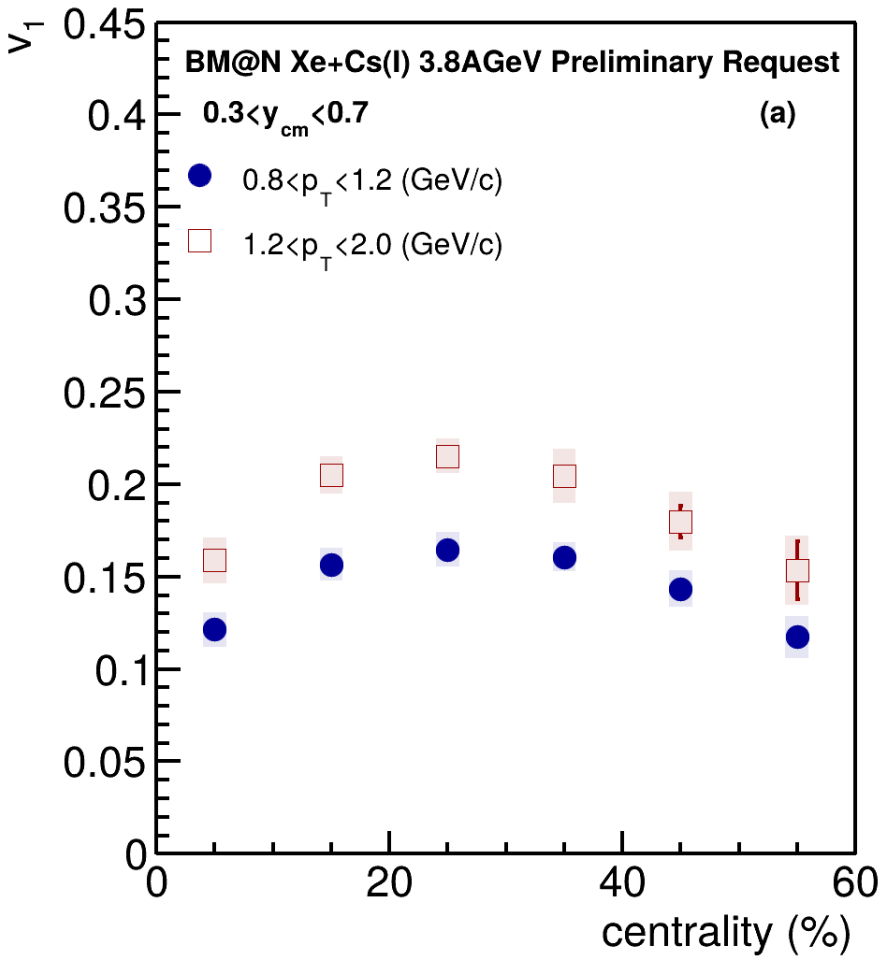
BM@N Xe+Cs(I) 3.8AGeV Preliminary Request
0.3<y_cm<0.7
(a)
0.8<p_T<1.2 (GeV/c)
1.2<p_T<2.0 (GeV/c)
v_1
centrality (%)

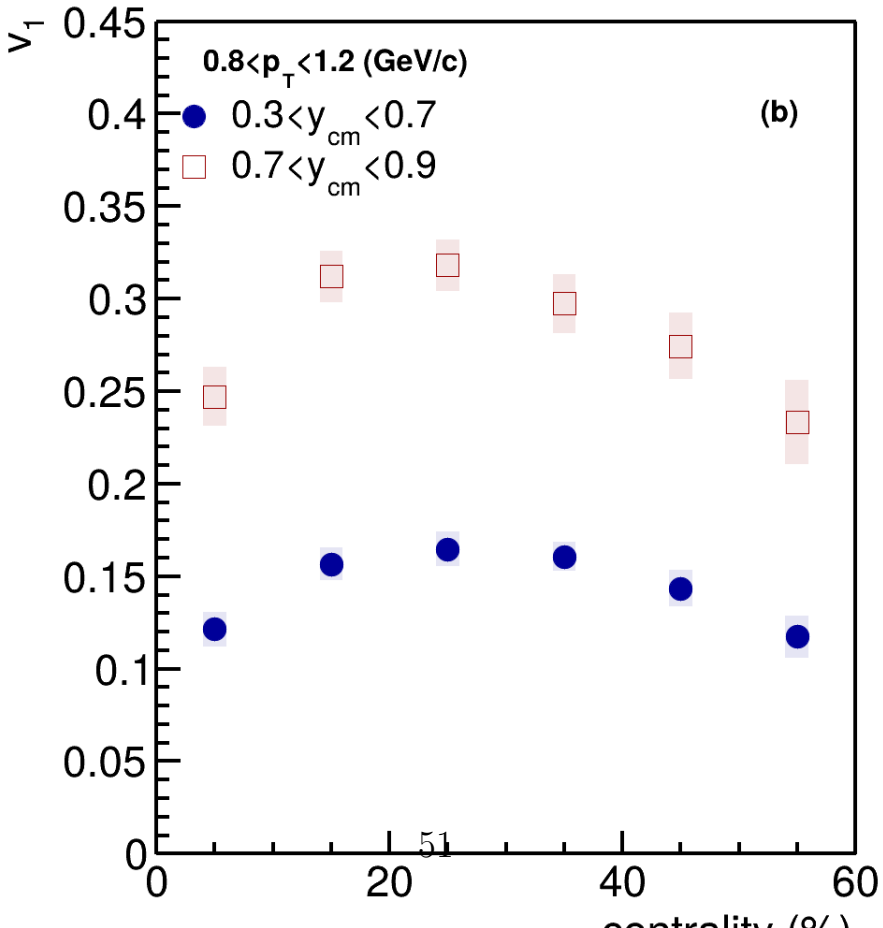
0.8<p_T<1.2 (GeV/c)
0.3<y_cm<0.7
0.7<y_cm<0.9
(b)
v_1

References

1. *Mamaev M.* [et al.]. Directed flow of protons in Xe+Cs(I) collisions at 3.8 AGeV // BM@N Analysis Note. — 2024. — P. 58.
2. *Sorensen A.* [et al.]. Dense nuclear matter equation of state from heavy-ion collisions // Prog. Part. Nucl. Phys. — 2024. — Vol. 134. — P. 104080.
3. *Poskanzer A. M.*, *Voloshin S. A.* Methods for analyzing anisotropic flow in relativistic nuclear collisions // Phys. Rev. C. — 1998. — Vol. 58. — P. 1671–1678.
4. *Voloshin S.*, *Zhang Y.* Flow study in relativistic nuclear collisions by Fourier expansion of azimuthal particle distributions // Zeitschrift for Physik C Particles and Fields. — 1996. — May. — Vol. 70, no. 4. — P. 665–671.
5. *Voloshin S. A.*, *Poskanzer A. M.*, *Snellings R.* Collective phenomena in non-central nuclear collisions // Landolt-Bornstein / ed. by R. Stock. — 2010. — Vol. 23. — P. 293–333. — arXiv: `0809.2949 [nucl-ex]`.
6. *Selyuzhenkov I.*, *Voloshin S.* Effects of non-uniform acceptance in anisotropic flow measurement // Phys. Rev. C. — 2008. — Vol. 77. — P. 034904.
7. *Liu H.* [et al.]. Sideward flow in Au + Au collisions between 2-A-GeV and 8-A-GeV // Phys. Rev. Lett. — 2000. — Vol. 84. — P. 5488–5492.
8. *Pinkenburg C.* [et al.]. Elliptic flow: Transition from out-of-plane to in-plane emission in Au + Au collisions // Phys. Rev. Lett. — 1999. — Vol. 83. — P. 1295–1298.
9. *Chung P.* [et al.]. Differential elliptic flow in 2-A-GeV - 6-A-GeV Au+Au collisions: A New constraint for the nuclear equation of state // Phys. Rev. C. — 2002. — Vol. 66. — P. 021901.
10. *Reisdorf W.* [et al.]. Systematics of azimuthal asymmetries in heavy ion collisions in the 1 A GeV regime // Nucl. Phys. A. — 2012. — Vol. 876. — P. 1–60.

11. *Adamczewski-Musch J.* [et al.]. Proton, deuteron and triton flow measurements in Au+Au collisions at $\sqrt{s_{\rm NN}} = 2.4$ GeV // Eur. Phys. J. A. — 2023. — Vol. 59, no. 4. — P. 80.

12. *Adam J.* [et al.]. Flow and interferometry results from Au+Au collisions at $\sqrt{s_{NN}} = 4.5$ GeV // Phys. Rev. C. — 2021. — Vol. 103, no. 3. — P. 034908.

13. *Abdallah M. S.* [et al.]. Disappearance of partonic collectivity in $\sqrt{s_{\rm NN}} = 3$ GeV Au+Au collisions at RHIC // Phys. Lett. B. — 2022. — Vol. 827. — P. 137003.

14. *Danielewicz P.*, *Lacey R.*, *Lynch W. G.* Determination of the equation of state of dense matter // Science. — 2002. — Vol. 298. — P. 1592–1596.

15. *Senger P.* Heavy-Ion Collisions at FAIR-NICA Energies // Particles. — 2021. — Vol. 4, no. 2. — P. 214–226.

16. *Le Fèvre A.* [et al.]. Constraining the nuclear matter equation of state around twice saturation density // Nucl. Phys. A. — 2016. — Vol. 945. — P. 112–133.

17. *Oliinychenko D.* [et al.]. Sensitivity of Au+Au collisions to the symmetric nuclear matter equation of state at 2–5 nuclear saturation densities // Phys. Rev. C. — 2023. — Vol. 108, no. 3. — P. 034908. — arXiv: `2208.11996 [nucl-th]`.

18. *Mamaev M.*, *Taranenko A.* Toward the System Size Dependence of Anisotropic Flow in Heavy-Ion Collisions at $\sqrt{s_{NN}}$= 2–5 GeV // Particles. — 2023. — Vol. 6, no. 2. — P. 622–637.

19. *Afanasiev S.* [et al.]. The BM@N spectrometer at the NICA accelerator complex. — 2023. — Dec. — arXiv: `2312.17573 [hep-ex]`.

20. *Sharma S. R.* First-Order Event Plane Correlated Directed and Triangular Flow from Fixed-Target Energies at RHIC-STAR // Universe. — 2024. — Vol. 10, no. 3. — P. 118.

21. *Loizides C.*, *Nagle J.*, *Steinberg P.* Improved version of the PHOBOS Glauber Monte Carlo // SoftwareX. — 2015. — Vol. 1/2. — P. 13–18.

22. Centrality determination using the Glauber model in Xe-Xe collisions at $\sqrt{s_{\rm NN}} = 5.44$ TeV. — 2018.

23. *Rogly R.*, *Giacalone G.*, *Ollitrault J.-Y.* Reconstructing the impact parameter of proton-nucleus and nucleus-nucleus collisions // Phys. Rev. C. — 2018. — Vol. 98, no. 2. — P. 024902.

24. *Parfenov P.* [et al.]. Relating Charged Particle Multiplicity to Impact Parameter in Heavy-Ion Collisions at NICA Energies // Particles. — 2021. — Vol. 4, no. 2. — P. 275–287.

25. *Frankland J. D.* [et al.]. Model independent reconstruction of impact parameter distributions for intermediate energy heavy ion collisions // Phys. Rev. C. — 2021. — Vol. 104, no. 3. — P. 034609.

26. *Plotnikov V. A.*, *Kapishin M. N.* Evaluation of Trigger Efficiency in the BM@N Experiment Session with a Beam of Xenon Ions with a Kinetic Energy of 3.8 AGeV // Phys. Part. Nucl. Lett. — 2025. — Vol. 22, no. 6. — P. 1406–1415.

27. *Selyuzhenkov I.*, *Kreis L.* QnTools -A framework for multi-differential acceptance correction and anisotropic flow analysis // https://github.com/HeavyIonAnalysis/Q 2024.

28. *Nara Y.* JAM: an event generator for high energy nuclear collisions // EPJ Web Conf. / ed. by B. Pattison [et al.]. — 2019. — Vol. 208. — P. 11004.

29. *Nara Y.*, *Ohnishi A.* Mean-field update in the JAM microscopic transport model: Mean-field effects on collective flow in high-energy heavy-ion collisions at $\sqrt{s_{\mathrm{NN}}} = 2$ - 20 GeV energies // Phys. Rev. C. — 2022. — Vol. 105, no. 1. — P. 014911.

30. *Nara Y.*, *Maruyama T.*, *Stoecker H.* Momentum-dependent potential and collective flows within the relativistic quantum molecular dynamics approach based on relativistic mean-field theory // Phys. Rev. C. — 2020. — Vol. 102, no. 2. — P. 024913.

31. *Parfenov P.* Model Study of the Energy Dependence of Anisotropic Flow in Heavy-Ion Collisions at $\sqrt{s_{NN}} = 2$–4.5 GeV // Particles. — 2022. — Vol. 5, no. 4. — P. 561–579.